PHYSICAL REVIEW FLUIDS **4**, 044605 (2019)

Intense sound radiation by high-speed flow: Turbulence structure, gas properties, and near-field gas dynamics

David A. Buchta[1] and Jonathan B. Freund[2,3,*]
[1]*Coordinated Science Laboratory, University of Illinois at Urbana-Champaign, Urbana, Illinois 61801, USA*
[2]*Department of Mechanical Science and Engineering, University of Illinois at Urbana-Champaign, Urbana, Illinois 61801, USA*
[3]*Department of Aerospace Engineering, University of Illinois at Urbana-Champaign, Urbana, Illinois 61801, USA*

(Received 9 August 2018; published 11 April 2019)

Free-shear-flow turbulence with sufficiently fast advection speeds radiates Mach waves, with steepened and skewed pressure profiles. These form within about a mixing layer thickness and dominate the sound field. Their generation and propagation is investigated through comparison of numerical simulations of a temporally developing mixing layer with a series of model-flow simulations designed to isolate physical mechanisms. The first of these are numerical simulations of nonlinearly saturating instability waves, which despite being much simpler than corresponding turbulence reproduce key features of the sound. Motivated in part by this agreement, instability analysis is used to motivate the inclusion of artificial sources in turbulence simulations that are designed to induce specific alterations to the turbulence structures, leaving most of its broadband spectrum unchanged. Comparisons show how insensitive the radiation is to the particular structure. To assess how strongly the near-field sound is coupled to the turbulence, a high dilatational dissipation is imposed to suppress the waves. This significantly reduces radiated pressure intensity, but little changes the Reynolds stresses ($<8\%$), which supports a source-plus-sound perspective. Given this, a low-dimensional nonlinear gas-dynamic mechanism is proposed for the generation and near-field propagation of the waves. The analysis uses a second-order wavy-wall asymptotic solution, and it reproduces the key observations: the sound-field structure, pressure skewness, and even the radiated pressure levels to within a factor of 2.

DOI: 10.1103/PhysRevFluids.4.044605

I. INTRODUCTION

High-speed shear-flow turbulence is well known to radiate intense directional sound, which has consequences. Near jet engines, such as those currently on some military aircraft, it causes hearing loss for personnel. Furthermore, spurious sound radiated by supersonic boundary layers has long been known to potentially mask mechanisms in studies of turbulence transition [1]. Unlike at subsonic speeds, the near field is dominated by shocklike waves with fronts approximately perpendicular to the direction of peak sound intensity [2–4]. For jets, this angle θ is typically between 30° and 50° from the jet axis, depending on the speed. It can be anticipated that the character of acoustic radiation should indeed change when the turbulence structures advect at supersonic speeds, which provides them a wave-number-frequency makeup that can directly couple to propagating solutions of a scalar wave equation, with the implication that they can be particularly efficient acoustic sources [5,6]. In contrast, at lower speeds, it is the more subtle changes to the

---

[*] jbfreund@illinois.edu

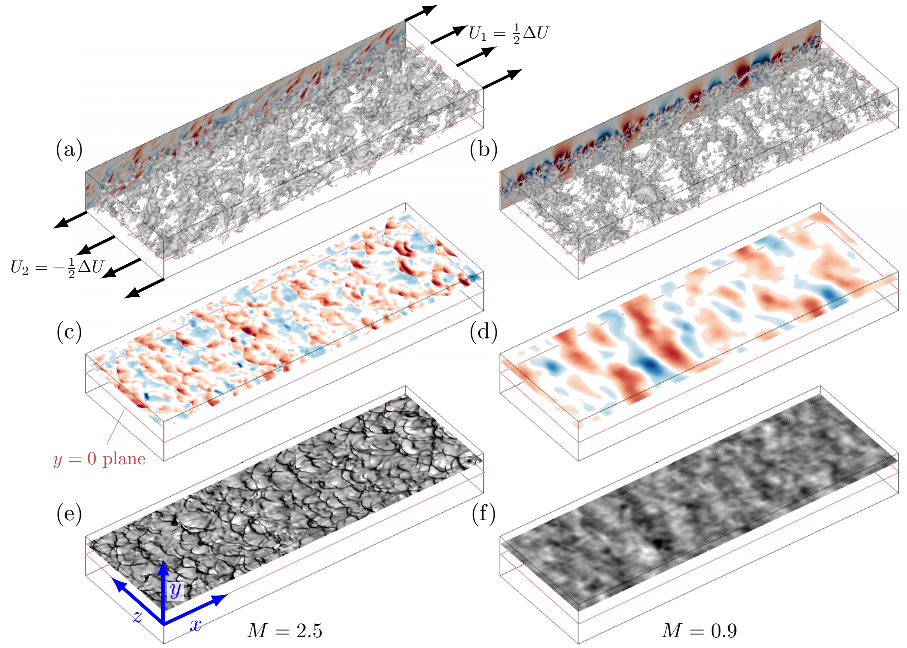

FIG. 1. Iso-surfaces (iso.) of pressure ($p_{\text{iso.}} - p_\infty = -0.027\,\rho_\infty \Delta U^2$) when $\delta_m/\delta_m^o = 10$: (a) $M = 2.5$ and (b) $M = 0.9$. [(c), (d)] Corresponding pressure at $y/\delta_m = 4$ with $p = p_\infty \pm 0.4\,\rho_\infty \Delta U^2$ for $M = 2.5$ and $p_\infty \pm 0.1\,\rho_\infty \Delta U^2$ for $M = 0.9$. Positive perturbations are red. [(e), (f)] Dilatation at $y/\delta_m = 4$ with $\nabla \cdot \mathbf{u} = \pm 0.1\ \Delta U/\delta_m$ for $M = 2.5$ and (f) $\pm 0.001\ \Delta U/\delta_m$ for $M = 0.9$. Compressions are black. Only a small part (one-eighth) of the simulation domain in the y direction is shown.

energetic structures that couple with propagating waves [6,7]. Phillips [8] anticipated "eddy Mach waves" at angles near the Mach angle anticipated based on the speed of advecting turbulence structures. Based on a linear model, such waves should orient with the outgoing characteristics angle

$$\theta = \sin^{-1}\left(\frac{c_\infty}{U_1 - U_c}\right), \tag{1}$$

which for advecting turbulence is based on the relative advection speed $U_1 - U_c > c_\infty$ for free-stream (or jet) velocity U_1 and the nominal eddy velocity U_c. Murray and Lyons [9] measured the distribution of wave orientations for jets and used (1) to infer the corresponding distribution of source speeds, finding agreement with measurements [10,11]. Similarly, direct numerical simulations (DNS) of temporally developing mixing layers also show a range of compression wave orientations near the turbulence [12]. The distribution of wave angles (and wave strengths) lead to nonlinear interactions; distinct waves merge as they propagate [12]. Figures 1(a), 1(c) and 1(e) show an example from a Mach $M = 2.5$ temporally developing free-shear turbulent flow we study. These have Reynolds number up to $\text{Re}_{\delta_m} = 2100$ and Mach numbers $M = 0.9$ and 2.5, based on the difference of the free-stream velocities $\Delta U = U_1 - U_2$, the momentum thickness δ_m, and ambient speed of sound c_∞. They were initialized with random perturbations to a laminar profile, which grows to be 35 times its initial thickness δ_m^o in a spanwise- and streamwise-periodic computational domain ($L_x = 1536\,\delta_m^o$ and $L_z = 512\,\delta_m^o$), with absorbing far-field boundary conditions at $\pm L_y/2 = 800\,\delta_m^o$. After an initial transient, during which the turbulence becomes approximately statistically stationary, we analyze data from $\delta_m(t) = 10\,\delta_m^o$ to $35\,\delta_m^o$. Many details of the methods and results from these simulations are reported elsewhere [12,13]; here we are considering some specific new questions. The sound field appears, as expected, to be dominated by thin shocklike features oriented at approximately the expected Mach angle [14,15], as previously analyzed for this configuration [12]. Still, it includes additional peculiarities. For $M \gtrsim 2.5$, the pressure is positively skewed, often with skewness $S_k \gtrsim 0.4$ [12], matching that commonly measured near round jets [4,16,17]. These both suggest that nonlinear mechanisms underlie the generation and affect the propagation of these waves. Past analysis of this flow shows that near the $M = 2.5$ turbulence, nonlinear effects are significant in the transport budget of S_k within $y \lesssim 20\,\delta_m$ from the source, where δ_m is the momentum thickness of the shear layer [12]. Though the basic mechanism of Mach-wave generation and propagation is understood for idealized flows [18], the sound generated by turbulence has additional complexity, particularly its intricate three-dimensional pressure field with significant S_k.

Wave-packet models, which are motivated by the growth and decay phenomenology of instability waves, have been proposed to provide mechanistic models of noise sources in free-shear flows [19–21], and they are successful. The far-field sound intensity of supersonic advecting wave packets, in particular, follows the expected high-speed M^3 scaling [19], which is consistent with general theoretical results [5] and data [22,23]. Unlike subsonically advecting wave packets, whose sound is strongly sensitive to the space-time details of the wave packet, the radiation efficiency for supersonic advection depends mainly on the Mach number and not on the wave-packet structure *per se* [24], though a weak dependence on structure has been observed [25]. Despite the reasonable success of linear wave packets to predict the levels and peak radiation direction [26–29], discrepancies in the intensity remain unresolved. On top of their limitations in describing turbulence, they also do not form shocklike waves and skewed pressure statistics, so prominent in observations. This suggests a role of nonlinear mechanisms, such as has been studied in detail for two-dimensional mixing layers, where it was found to be important [28]. For a broadbanded input, there are significant differences between solutions of the linearized equations and of the full equations, even for modes that contribute most to sound levels near jets, for which linear theory might be expected to be most successful [30]. The strength of the pressure waves radiated by high-speed flows is also strong enough that nonlinearity could alter its propagation [18,31,32], which has been quantified for turbulent jets [33,34]. Here we consider that finite-amplitude effects may also potentially be coupled to the underlying turbulence as it is generated.

Another partial description of Mach-wave radiation from turbulence is based on a wavy-wall flow analogy, where the flow speed and wall perturbation wavelength are taken to correspond to instability waves [15,35]. This can be seen as replacing the turbulence (or wave packet) by a kinematic boundary condition that radiates into the domain. As with the wave-packet models, this linear description is also limited in that it cannot reproduce some prominent features of the sound. However, within this framework, and in conjunction with turbulence DNS, we augment it to include additional nonlinear mechanisms. The first involves the finite displacement of the flow, which is modeled by the wall streamline in the wavy-wall model. In the corresponding asymptotic solution, second-order terms in the boundary conditions introduce harmonics [36–38]. The second is a consequence of the Navier-Stokes equations involving both nonlinear convection and equation of state effects. Convection mechanisms, involving $(\mathbf{u} \cdot \nabla \mathbf{u})$-like terms, are well understood to steepen waves as they propagate, leading to a standard N-wave [18]. However, this description is incomplete since, unlike for turbulence, the waves have antisymmetric positive and negative peaks and thus zero skewness ($S_k = 0$), so additional mechanisms must be responsible for radiating skewed pressure signals. Supersonic wave packets simulated in a uniform flow (supplying a finite amplitude of $p \approx 0.06\, p_\infty$ perturbation along the streamwise axis) do reproduce features like those observed in the sound radiated by a high-speed jet: large skewness ($S_k > 0.4$) and wave steepening [39]. However, it remains unclear if the essential nonlinearity arises from finite-fluid displacement, convection mechanisms, the equation of state, or some mix of these. The objective of this paper is to further examine nonlinear mechanisms of sound generation in high-speed flows, specifically their importance to sound radiation by turbulence. In particular, we seek to differentiate the nonlinear mechanisms that might lead to $S_k = 0$ N-waves from those that yield the $S_k \gtrsim 0.4$ waves observed near turbulence. Turbulence simulations provide a specific point of reference between the model mechanisms and turbulence sound sources.

In Sec. II, we simulate the sound and onset of nonlinearity from saturating instability modes. Their nascent sound with $S_k > 0$ is similar to that from turbulence. These simulations provide the connection between the flow speed, mode structure, and the effect of increasing nonlinearity on the radiated sound field. These observations are used in Sec. III to design source terms in auxiliary simulations that alter the turbulence structure of a $M = 2.5$ mixing layer to assess its role on the sound strength p'_{rms} and S_k. Section IV considers nonlinearity associated with the gas properties by modifying them. In particular, the gas is stiffened to assess the importance of the pressure-density nonlinearity in the equation of state. Similarly, the strength of two-way coupling between the strong sound and the turbulence is assessed using simulations with significantly increased dilatational dissipation. With this information, in Sec. V we introduce a weakly nonlinear wavy-wall model flow, informed by DNS, and use it to illustrate the nonlinear gas dynamics leading to behaviors observed for turbulence. As for high-speed flow turbulence, the model's radiation has $S_k > 0$ and depends mainly on the Mach number and perturbation amplitude, and it is relatively insensitive to spatial structure. Section VI provides a summary of the results.

II. ACOUSTIC RADIATION FROM NONLINEARLY SATURATING INSTABILITY WAVES

Before considering turbulence in the following section, the simulations in this section are designed to assess the onset of nonlinear source and sound mechanisms, before subsequent nonlinear effects obscure them. Linear theory is used to select initial conditions for these model-flow DNS. The Mach number range, $0.9 \leqslant M \leqslant 3.5$, was chosen to match the corresponding turbulence DNS [12] to facilitate subsequent comparisons. Figures 2(a) and 2(b) illustrate the basic behavior for such an instability for $M = 2.5$, with details of the setup following in this section. In this case, because of its $c_p < 0$ phase velocity, the selected linearly amplifying mode radiates mostly above the shear layer ($y > 0$) at the anticipated Mach angle (1). However, the pressure waves, which are initially harmonic with $S_k \approx 0$ [Fig. 2(b)], become increasingly positively skewed (peaks higher than the troughs) in Fig. 2(d). As the perturbation intensity

$$M_t(t) = \frac{(\overline{u'_i u'_i})^{1/2}}{c_\infty}, \tag{2}$$

based on u'_i velocity perturbations to the base flow measured at $y = 0$, increases exponentially in time [Figs. 3(a) and 3(b)], the S_k increases approximately linearly with M_t. This is true both at $y = 0$ and in the sound field, as shown in Figs. 3(c) and 3(d). By $t = 1000\delta^o_m/c_\infty$, a shock is nearly formed [Fig. 2(d)] by standard wave steepening (e.g., Ref. [31]). Yet, its tendency to also form positive S_k is not universal to wave steepening and requires additional explanation.

The stability of flows of this kind has been extensively analyzed [40–42], and further documentation of this specific configuration and the corresponding simulations are reported elsewhere [13]. The perturbations we consider have the usual form

$$\vec{q}(\mathbf{x}, t) = \varepsilon \vec{Q}(y) \exp[i(\alpha x + \beta z - \omega t)], \tag{3}$$

where $\vec{q} = [u', v', w', \rho', p']^{\mathrm{T}}$ and $\vec{Q} = [\hat{u}, \hat{v}, \hat{w}, \hat{\rho}, \hat{p}]^{\mathrm{T}}$. In the simulations, the initial amplitude is $\varepsilon = 10^{-3}$, which is sufficiently small for initial amplification to match growth predicted by the imaginary component ω_i of the eigenvalue $\omega = \omega_r + i\omega_i$. The corresponding phase speed is $c_p = \omega_r/\alpha$, whose difference from the free stream, $U_1 - c_p$, defines a nominal structure relative speed

$$U_c = (U_1 - c_p)\cos\phi, \tag{4}$$

where $\cos\phi = \alpha/\sqrt{\alpha^2 + \beta^2}$. A similar relation has been used to explain the acoustic inefficiency of oblique subsonic modes with $U_c < c_\infty$ [43]. In Figs. 2(a) and 2(c), we see Machlike waves with $\theta \approx 39°$, which correspond to the instability eigenvalue. However, below the shear layer ($y < 0$), the

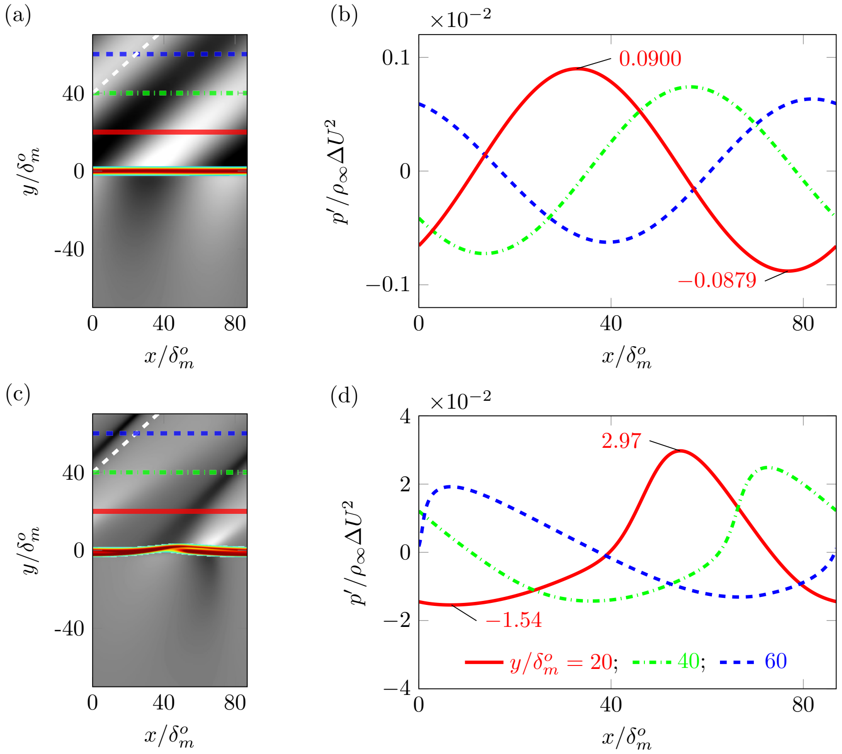

FIG. 2. Direct numerical simulation of the unstable mode with $(\alpha, \beta) = (0.289, 0)/\delta_m^o$, where $\delta_m^o = \delta_m(t = 0)$, for $M = 2.5$: [(a), (b)] $\delta_m = 1.25\delta_m^o$ and [(b), (d)] $\delta_m = 1.5\delta_m^o$; panels (a) and (c) show dilatation (grays: $|\boldsymbol{\nabla} \cdot \mathbf{u}| < 0.1\,\Delta U/\delta_m$) and vorticity (color: $\boldsymbol{\nabla} \cdot\ \mathbf{u} < 0.5\,\Delta U/\delta_m$) fields and corresponding streamwise pressure in panels (b) and (d) at the indicated y locations.

relative speed is subsonic $|(U_2 - c_p)\cos(\phi)| < c_\infty$, precluding Mach waves, though of course there are corresponding $c_p > 0$ modes that could coexist with these and that would radiate predominantly into the $y < 0$ region. Saturating two-dimensional instabilities radiate more intensely with larger S_k than $\phi > 0$ oblique modes. Contributions to S_k transport in turbulence DNS support a similar observation: Three-dimensional (in-plane) contributions to S_k were not significant [12].

Subsonic flow behavior is counter to this: The most unstable mode has $\beta = 0$ and, also similar to developed turbulence, they have negative S_k inside the shear layer, as seen in Fig. 3(c). The pressure decreases exponentially for small $|y|$ (not shown), consistent with evanescent radiation, and waves with $S_k \approx 0$ [Fig. 3(d)] persist to larger $|y|$, consistent with those near mixing layer turbulence [12]. Likewise, Fig. 4(a) shows that for the modes we consider (summarized in Table III in Appendix A), the radiated sound-field intensity shows both U^8 and U^3 scaling, consistent with theoretical considerations [5,7] and observations for turbulence [12]. Along with increasing intensity, the corresponding skewness also increases with U [Fig. 4(b)], consistent with trends observed in the turbulence. However, the relation of U to advection speed of turbulent structures is not necessarily simple, especially in high-Mach-number flows, for which turbulence structures are less correlated across the mixing layer. To anticipate its impact, we consider a range of possible advection speeds based on the local mean flow speed at $y = 0$, $\pm\delta_m$, and $\pm 2\delta_m$. These reflect the turbulence advection speeds based on their y-dependent space-time correlations (see Appendix C). This y range includes the most intense velocity fluctuations (see Fig. 6), and corresponding velocities also encompass linear instability phase velocities. These observations, confirming multiple similarities between radiation from saturating instabilities and turbulence, motivate the following section, which

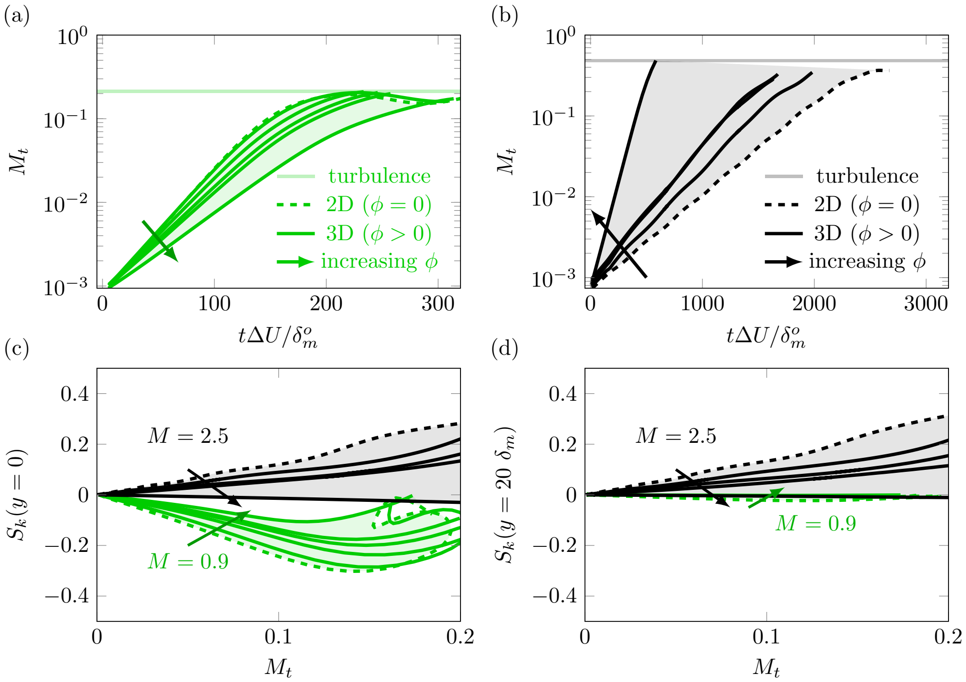

FIG. 3. [(a), (b)] Growth of M_t (2) at $y = 0$ for the discrete modes of Table III in Appendix A: (a) $M = 0.9$ and (b) $M = 2.5$. For reference, the horizontal lines indicate the approximately stationary M_t from corresponding turbulence DNS [12]. [(c), (d)] Dependence of pressure skewness on disturbance amplitude M_t: (c) $y = 0$ and (d) $y = 20\,\delta_m$.

examines the effect of a narrow-band forcing of linear-mode-like structures in the turbulence to assess sensitivity of radiated sound to structure. In doing this, we particularly assess the role of the oblique ($\phi \neq 0$) stability modes, which are most amplifying yet have subsonic velocity $U_c < c_\infty$, versus the supersonic $\phi = 0$ modes.

III. MODIFIED LARGE-SCALE TURBULENCE STRUCTURE

The saturating instabilities of the previous section radiate sound with signatures of nonlinear mechanisms similar to fully developed turbulence at similar conditions, depending on their relative speed. The visualizations for $M = 2.5$ and 0.9 in Fig. 1 also support a link to their structure, with the high-speed turbulence and its corresponding sound appearing more three-dimensional than the corresponding lower speed flow. However, the results also indicate that for fixed M the near-field pressure depends primarily on the mode's relative Mach number. Larger pressure fluctuations come from higher U/c_∞ and less oblique (more two-dimensional) modes, which are not the most amplified by linear mechanisms in higher speeds.

To quantify the role of structure itself on the radiated sound, we introduce an artificial source that reallocates perturbation energy between different types of structures, with the goal of otherwise minimally disrupting the flow. Similar modifications to the flow equations have been used, for example, to study the maintenance of wall turbulence [44]. Similarly, experiments with near-nozzle shear-layer excitation have probed noise generation mechanisms of large-scale structures, though with far less control over the specific excitation [45,46]. Here, energy is extracted from the most unstable oblique Fourier components, as predicted by linear theory, by a source added to the

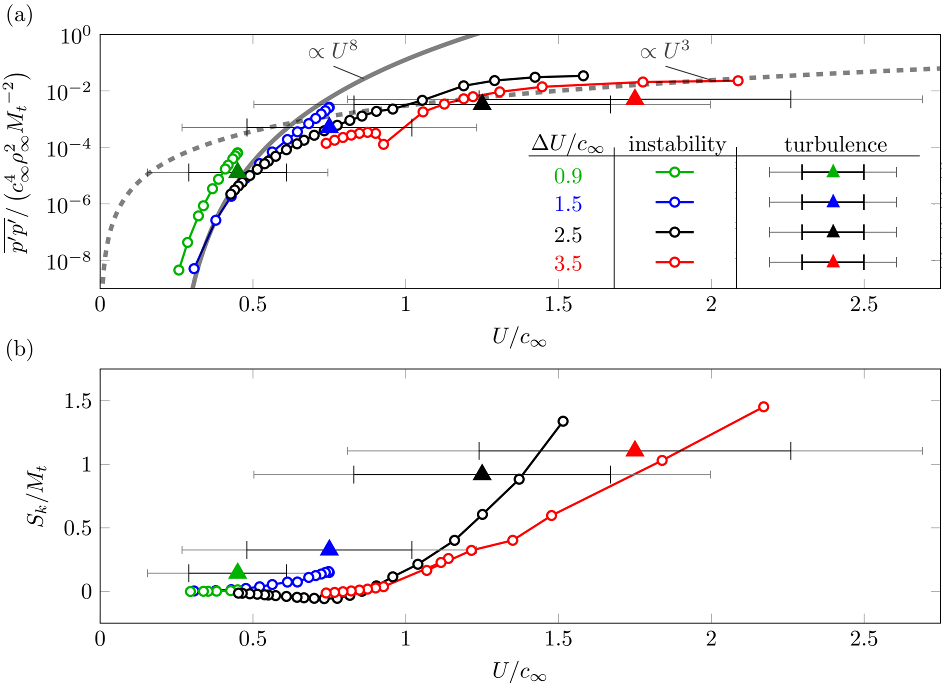

FIG. 4. Comparison of saturating instabilities and turbulence based on relative free-stream speeds: (a) pressure intensity and (b) pressure skewness at $y/\delta_m(t) = 20$. For saturating instabilities, the relative velocity $U = U_c$ is defined using (4). For turbulence, an anticipated range of advection velocities are based on y-location mean speed $\bar{u}(y)$ (see text). The results are shown for $U = \Delta U/2 - \bar{u}(y)$: $y = 0$ (symbol), $y = \pm 1\delta_m$ (inner bar), and $y = \pm 2\delta_m$ (outer bar). Solid and dashed curves in (a) are $\propto U^8$ and $\propto U^3$, respectively, as labeled.

$N(\vec{q}) = 0$ flow equations (for $\vec{q} = [\rho u, \rho v, \rho w, \rho, \rho e]^{\mathrm{T}}$):

$$N(\vec{q}) = -A\omega_i W(y)\begin{bmatrix} \rho(u-u^t) + u(\rho-\rho^t) \\ \rho(v-v^t) + v(\rho-\rho^t) \\ \rho(w-w^t) + w(\rho-\rho^t) \\ (\rho-\rho^t) \\ \frac{(p-p^t)}{(\gamma-1)} + \rho u_i(u_i - u_i^t) + \frac{1}{2}u_i u_i(\rho-\rho^t) \end{bmatrix}, \tag{5}$$

where A is a strength parameter, ω_i is the growth rate of the most unstable mode from (3), and $W(y)$ restricts its support to $|y| \lesssim \frac{1}{2}\delta_{99}(t)$:

$$W(y) = \frac{1}{2}\left\{\tanh\left[\frac{5}{\delta_m(t)}\left(y + \frac{\delta_{99}(t)}{2}\right)\right] - \tanh\left[\frac{5}{\delta_m(t)}\left(y - \frac{\delta_{99}(t)}{2}\right)\right]\right\}. \tag{6}$$

In (6), δ_{99} is the distance between the y locations having 99% of ambient flow speeds. Each q component of $\vec{q}$ is discrete Fourier transformed in the periodic x and z directions (see Fig. 1):

$$\hat{q}_{k_x k_z}(y) = \frac{1}{N_x N_z}\sum_{m=0}^{N_z-1}\sum_{n=0}^{N_x-1} q_{nm}(y)\exp\left[-\frac{2\pi i k_x n}{N_x}\right]\exp\left[-\frac{2\pi i k_z m}{N_z}\right]. \tag{7}$$

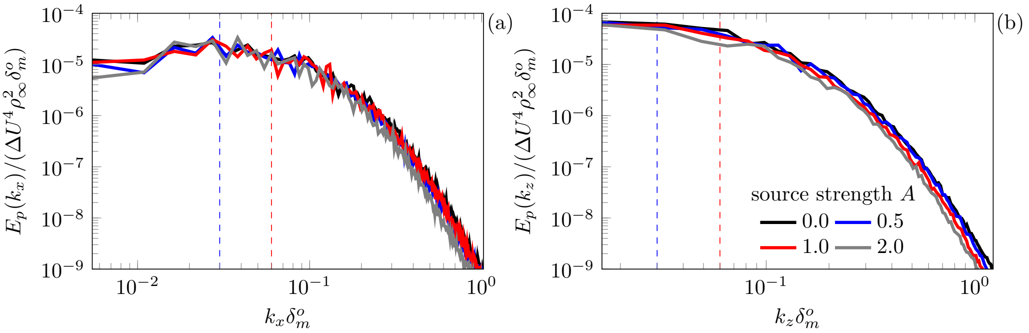

FIG. 5. Effect of source strength A on the $y = 0$ pressure spectra when $\delta_m(t)/\delta_m^o = 10$: (a) streamwise and (b) spanwise directions. The dashed lines indicate the initial and final modulated target wave numbers.

The superscript t in (5) indicates the target field, with corresponding transform

$$\hat{q}^t_{k_x k_z} = \begin{cases} 0, & k_x = k_1, k_z = |k_2| \quad \leftarrow \text{damps oblique} \\ \hat{q}_{k_x k_z}\sqrt{\frac{E_{1,0}+E_{1,2}+E_{1,-2}}{E_{1,0}}}, & k_x = k_1, k_z = 0 \quad \leftarrow \text{excites } \beta = 0 \\ \hat{q}_{k_x k_z}, & \text{otherwise} \quad \leftarrow \text{leave others unchanged} \end{cases}. \tag{8}$$

The mode energy is $E_{i,j} = \hat{q}_{k_i k_j}\hat{q}^\star_{k_i k_j}$, where the $\star$ indicates complex conjugate. The wave-number pair $(k_1, \pm k_2)$ is the most linearly amplified mode pair (supported by the discretization at the time forcing is initiated). For the $M = 2.5$ case, it is $(k_1, \pm k_2) = (0.289, \pm 0.537)\,\delta_m(t)$, with corresponding growth rate $\omega_i = 0.096\,\Delta U/\delta_m(t)$. The coefficients in (8) are designed to conserve $\sum E_{i,j}$. We note that the unstable linear mode depends on the momentum thickness, which grows approximately linearly in time; k_1 and k_2 change in time to track this dependence.

Any source terms such as in (5) can potentially generate sound directly, which is confirmed by an acoustic analogy formulation [6] in Appendix B to be less consequential than the direct turbulence sound sources. Thus, changes in the sound are due to changes in the turbulence caused by the forcing, not the forcing itself.

The numerical methods for (5) are standard high-order finite-difference methods and reported in full elsewhere [13]. The domain of size $L_x \times L_y \times L_x = 1536\,\delta_m^o \times 800\,\delta_m^o \times 192\,\delta_m^o$ is discretized with $N_x \times N_y \times N_z = 1536 \times 801 \times 192$ uniformly spaced mesh points. The turbulence, initialized from broadband velocity fluctuations [47], develops naturally until $\delta_m(t) = 5\,\delta_m^o$. By design, forcing the turbulence to the two-dimensional target state increases the z correlations [13]. However, we emphasize that the effect on the overall range of turbulence scales is modest: The near-field pressure spectra in Fig. 5 appear unchanged aside from the depletion in energy near $k = k_1$ due to (8), which is more pronounced for larger A. Otherwise, there is a broad range of scales similar to the baseline case.

Since the energy is removed from the most amplified mode, it is anticipated that the shear layer growth rate will be suppressed, though this too is modest. Between times with $\delta_m = 5\,\delta_m^o$ to $10\,\delta_m^o$, growth rate decreases from $\dot{\delta}_m = 0.0066\,\Delta U$ for $A = 0$ in (5) to $0.0042\,\Delta U$ for $A = 2$. The Reynolds stresses shown in Figs. 6(a)–6(d) and mean u velocity (not shown) are similarly insensitive for $A \lesssim 1$ [13].

However, despite these modest changes to the turbulence intensity and structure, Fig. 7 shows that the sound fundamentally changes for $A = 1$. Spanwise correlated pressure waves are obvious, yet they are only modestly more intense and skewed than for $A = 0$. Figure 8(a) shows that the intensity increases by only a factor of 2 even for the most strongly forced $A = 2$ case. That spanwise correlation might increase acoustic efficiency is not unexpected, especially based on the instability mode sources in Sec. II. There it was shown that $\beta = 0$ modes have $U/c_\infty > 1$, which leads to larger pressure fluctuations and $S_k > 0$.

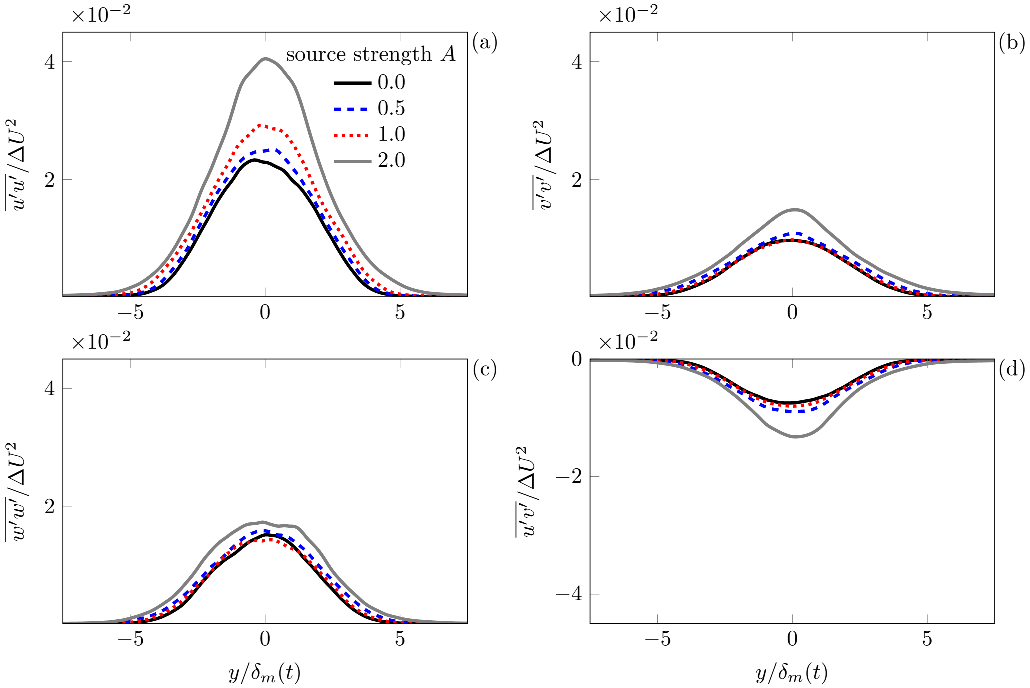

FIG. 6. Effect of the source strength A on the Reynolds stresses: (a) $\overline{u'u'}$, (b) $\overline{v'v'}$, (c) $\overline{w'w'}$, and (d) $\overline{u'v'}$.

Despite the change in structure and intensity, there is only a 7% increase in S_k [Fig. 8(b)] within the turbulence, and S_k is insensitive to A beyond $y/\delta_m > \delta_{99}$. The metric

$$S_{k\,|y|>\delta_{99}} = \frac{1}{L_y - \delta_{99}} \int_{|y|>\delta_{99}}^{L_y} S_k \, dy \tag{9}$$

only varies from $S_{k\,|y|>\delta_{99}} = 0.456$ for $A = 0$ to $S_{k\,|y|>\delta_{99}} = 0.485$ for $A = 2$, despite the increase in the turbulence intensities (Fig. 6, especially for $A = 2$). The results of simply depleting ($A = 1$) and enhancing ($A = -1$) the energy in the three-dimensional unstable modes, without corresponding

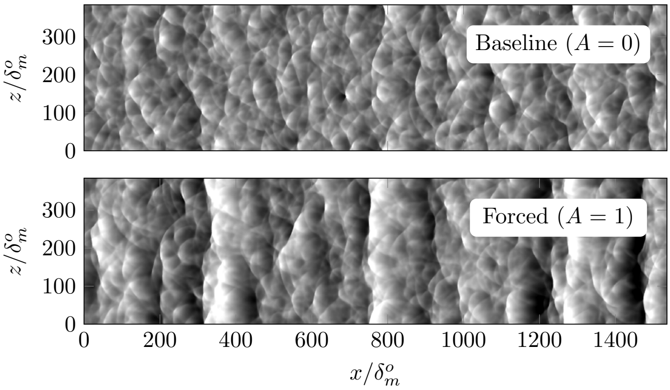

FIG. 7. Effect of the source strength on the sound-field pressure visualized with gray levels spanning $-0.025 < p'/(\Delta U^2 \rho_\infty) < 0.025$ for $M = 2.5$ at $y/\delta_m(t) = 10$ when $\delta_m(t)/\delta_m^o = 10$.

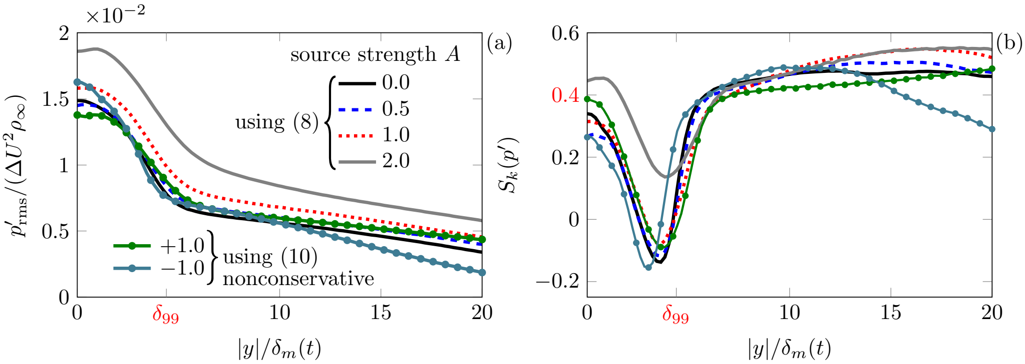

FIG. 8. Effect of source strength A on the pressure (a) intensity and (b) skewness for conservative forcing by (8) and nonconservative forcing by (10).

reallocation of the energy, which is accomplished by the source

$$\hat{q}^t_{k_xk_z} = \begin{cases} 0, & k_x = k_1, k_z = |k_2| \quad \leftarrow \text{damps oblique} \\ \hat{q}_{k_xk_z}, & \text{otherwise} \quad \leftarrow \text{leave others unchanged} \end{cases}, \tag{10}$$

are also shown in Fig. 8. For energy removal with $A = 1$, the pressure intensity at all y is less than its corresponding $A = 1$ reallocation using (8), though S_k is essentially unchanged. This result also shows that further departures from strict conservation of $N(\vec{q}) = 0$ using (10) versus (8) has similar

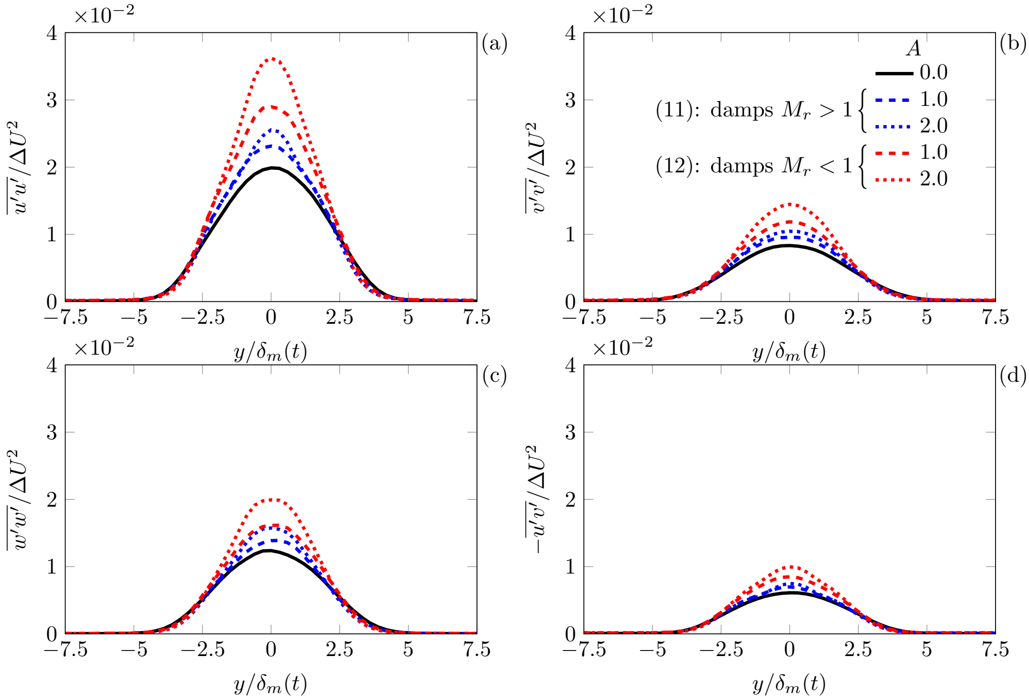

FIG. 9. Effect of the advection-based sources on the Reynolds stresses: (a) $\overline{u'u'}$, (b) $\overline{v'v'}$, (c) $\overline{w'w'}$, and (d) $-\overline{u'v'}$.

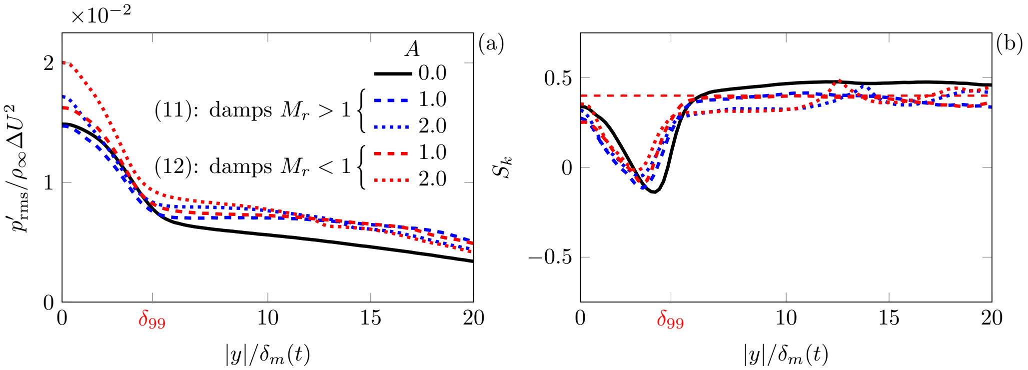

FIG. 10. Effect of the advection-based source modification on the pressure (a) intensity and (b) skewness.

radiation as the baseline $A = 0$. When the energy is added ($A = -1$), we observe little change in intensity and S_k up to $y < 10\delta_m$. Beyond $y \gtrsim 10\delta_m$, however, the trends diverge. The excited three-dimensional modes, which have subsonic advection speeds, support mainly evanescent disturbances and thus lower intensity further from their source. This is consistent with the instability modes of Sec. II.

The saturating instabilities of Sec. II show that intensity and skewness are particularly sensitive to U_c defined in (4). So, as an additional experiment, we deplete energy in modes based on their orientation-dependent speeds using

$$\hat{q}^t_{k_x k_z} = \begin{cases} 0, & \frac{\Delta U}{2} \frac{\alpha}{\sqrt{\alpha^2+\beta^2}} > 1 \quad \leftarrow \text{damps supersonic modes} \\ \hat{q}_{k_x k_z}, & \text{otherwise} \quad \leftarrow \text{leave others unchanged} \end{cases} \tag{11}$$

and

$$\hat{q}^t_{k_x k_z} = \begin{cases} 0, & \frac{\Delta U}{2} \frac{\alpha}{\sqrt{\alpha^2+\beta^2}} < 1 \quad \leftarrow \text{damps subsonic modes} \\ \hat{q}_{k_x k_z}, & \text{otherwise} \quad \leftarrow \text{leave others unchanged} \end{cases}. \tag{12}$$

Figure 9 confirms that changes to the Reynolds stresses are similar to the conservative (8) forcings. Likewise, the radiated pressure intensity shows little change and $S_k \gtrsim 0.4$ in Fig. 10.

Overall, altering the turbulence structure has little influence on the radiated pressure intensity and S_k. Unlike the saturating instabilities, on which the forcing was based, these high-speed flows still possess broadband, finite-amplitude turbulence fluctuations and sound with approximately the same characteristics is radiated. We next consider more directly the influence of gas-dynamic mechanisms on the radiated pressure by altering the gas itself. This leads to the wavy-wall model of Sec. V, which further isolates mechanisms leading to the sound intensity and its S_k, independent of structure.

IV. MODIFIED GAS PROPERTIES

The insensitivity of the Mach waves to turbulence structure suggests that their key features are more closely linked to the gas and its dynamics, which we alter by adjusting the gas stiffness. Similarly, we assess the influence of the waves on the turbulence by strongly damping them with a significantly increased bulk viscosity μ_b.

To adjust gas stiffness, we take

$$p = \rho e(\gamma - 1) - \gamma p^s, \tag{13}$$

TABLE I. Simulation parameters for stiffened equation of state.

Description	M	ΔU	p^s	c_∞	ρ_∞	$\frac{\partial p}{\partial \rho}\vert_{s_o}$	$\frac{1}{2}\frac{\partial^2 p}{\partial \rho^2}\vert_{s_o}$
Baseline	0.9	0.9	0.0	1.0	1.0	1.0	0.2
Stiffened	0.9^s	2.5	4.8	2.8	1.0	7.7	1.5
Baseline	2.5	2.5	0.0	1.0	1.0	1.0	0.2
Relaxed	2.5^s	0.9	– 0.6	0.4	1.0	0.1	0.03

which recovers an ideal gas for $p^s = 0$. This is a standard stiffened-gas model, which is typically parameterized first with a p_s that matches some shock speed then a γ to match the sound speed

$$c^2 \equiv \left.\frac{\partial p}{\partial \rho}\right|_s = \frac{\gamma(p+p^s)}{\rho}. \tag{14}$$

We adjust p^s to either stiffen (increase sound speed at fixed temperature) or relax the gas, keeping $\gamma = 1.4$. The parameters used, which are summarized in Table I, were selected based on airlike $M = 0.9$ and $M = 2.5$ cases. For one new case, the gas for $M = 0.9$ is stiffened, which is anticipated to augment any contribution of equation of state nonlinearity to the observed pressure intensity and skewness. Similarly, a $M = 2.5$ case is simulated with a relaxed gas, which is more easily compressed. The specific p^s and γ are selected such that the stiffened $M = 0.9$ (case 0.9^s) free-stream momentum flux $\rho\Delta U^2$ matches the baseline $M = 2.5$ case. Likewise, the free-stream momentum flux of the relaxed-gas $M = 2.5$ (case 2.5^s), matches that of the baseline $M = 0.9$ case.

Within the turbulence, the effect of gas stiffening is obvious in Fig. 11(a). Relative to the perfect gas limit, the stiffened gas has decreased density fluctuations for the same range of pressure fluctuations, and vice versa for the relaxed gas in Fig. 11(b). Of course, in turbulence, the distributions do not collapse exactly along any $p' \sim \rho'$ line, due to entropy fluctuations [48].

Despite these changes to the pressure-density distribution, Fig. 12 shows that the Reynolds stresses for the same Mach numbers are essentially unchanged from the perfect gas limit. The radiated pressure, quantified in Figs. 13(a) and 13(b), also show relative independence from gas stiffness, both for intensity and S_k, respectively. Even upon changing γ, Figs. 13(c) and 13(d) show little change to pressure statistics beyond $y \gtrsim \delta_{99}$.

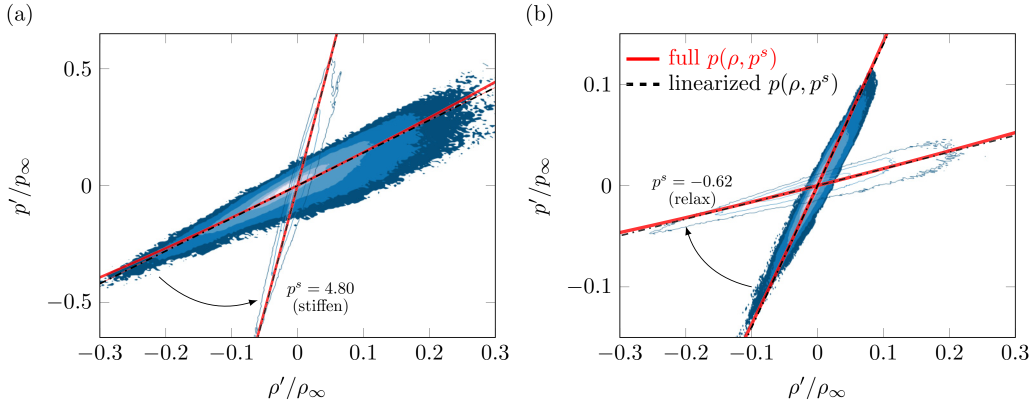

FIG. 11. Effect of gas stiffness on the joint pressure and density distribution at $y = 0$ when $\delta_m/\delta_m^o = 20$ for (a) $M = 0.9$ and (b) $M = 2.5$. Isolevels range from 1% to 90% and are filled for the baseline case ($p^s = 0$) and shown with just lines otherwise. For reference, isentropic approximations to the gas laws are provided: linearized (dashed) and full (solid).

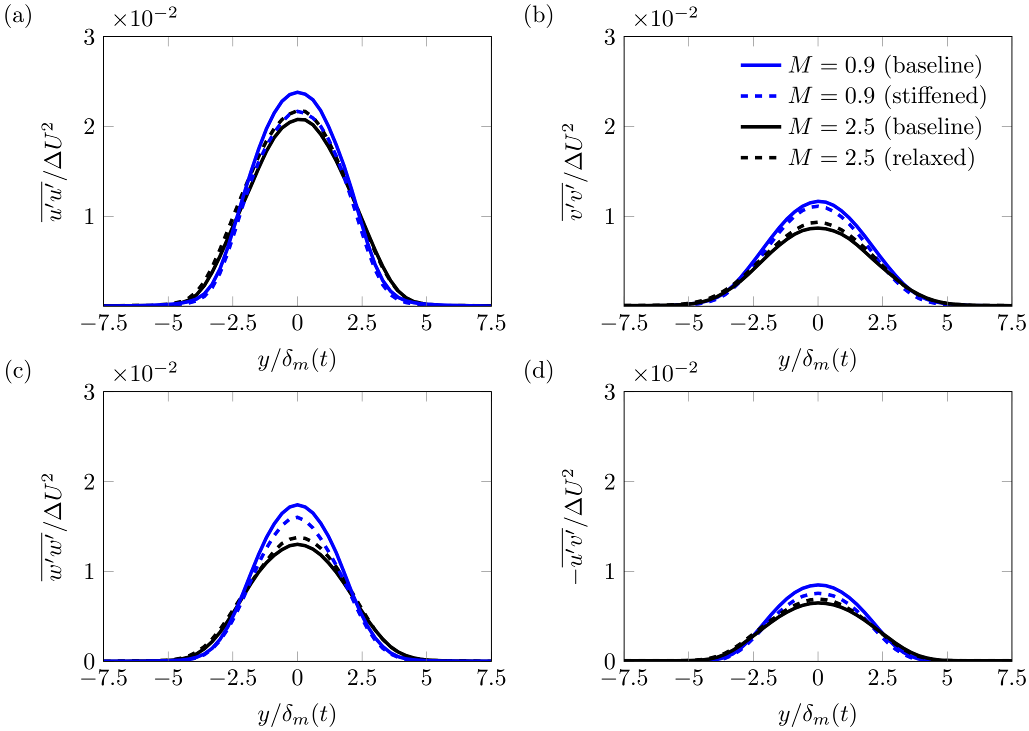

FIG. 12. Effect of gas stiffness on the Reynolds stresses: (a) $\overline{u'u'}$, (b) $\overline{v'v'}$, (c) $\overline{w'w'}$, and (d) $-\overline{u'v'}$.

The relatively small effect of significant gas stiffness on nonlinear dynamics is consistent with the expansion of pressure for uniform entropy,

$$p(\rho) = p(\rho_\infty) + (\rho - \rho_\infty)\frac{\partial p}{\partial \rho}\bigg|_{s_o} + \frac{1}{2}(\rho - \rho_\infty)^2 \frac{\partial^2 p}{\partial \rho^2}\bigg|_{s_o} + O[(\rho - \rho_\infty)^3], \tag{15}$$

where the linear- and quadratic-term coefficients are listed in Table I for the cases considered. Though (15) is approximate, the orientation (slope) of pressure-density distributions in Fig. 11 confirm that this is a reasonable model. However, significant curvature is not apparent, meaning that there is only a slight deviation from the linearized version of (15) in Fig. 11(b), and the nonlinearity of (15) is inconsequential. Other gas-dynamic effects are more important for S_k and intensity.

Gas stiffness is not a compressibility effect *per se* since it does not directly affect $\nabla \cdot \mathbf{u}$, and indeed Fig. 14(a) confirms its negligible effect on dilatation for the $M = 2.5$ relaxed-gas case. To confirm that the intense near-field pressure waves do not couple strongly back into the turbulence dynamics of the source, we suppress them by increasing the dilatational dissipation via the bulk viscosity μ_b in the viscous stress tensor

$$\sigma_{ij} = \mu\left(\frac{\partial u_i}{\partial x_j} + \frac{\partial u_j}{\partial x_i} - \frac{2}{3}\delta_{ij}\frac{\partial u_k}{\partial x_k}\right) + \mu_b \delta_{ij}\frac{\partial u_k}{\partial x_k}$$

from its standard-case value $\mu_b = 0$ up to 100μ. Though ideal gases are thought to have large ranges of μ_b ($\mu_b/\mu = 0$ to 1000 [49]), and its effect has been studied for turbulence dynamics in relatively extreme conditions [50,51], the present numerical experiments use μ_b simply as a means to assess the suppression of $\nabla \cdot \mathbf{u}$ on the turbulence.

Despite strong damping of the radiation [Fig. 14(a) through 14(d)], the turbulence stresses are virtually unchanged, with maximum change of +8% for $\overline{u'u'}$. This is consistent with observations

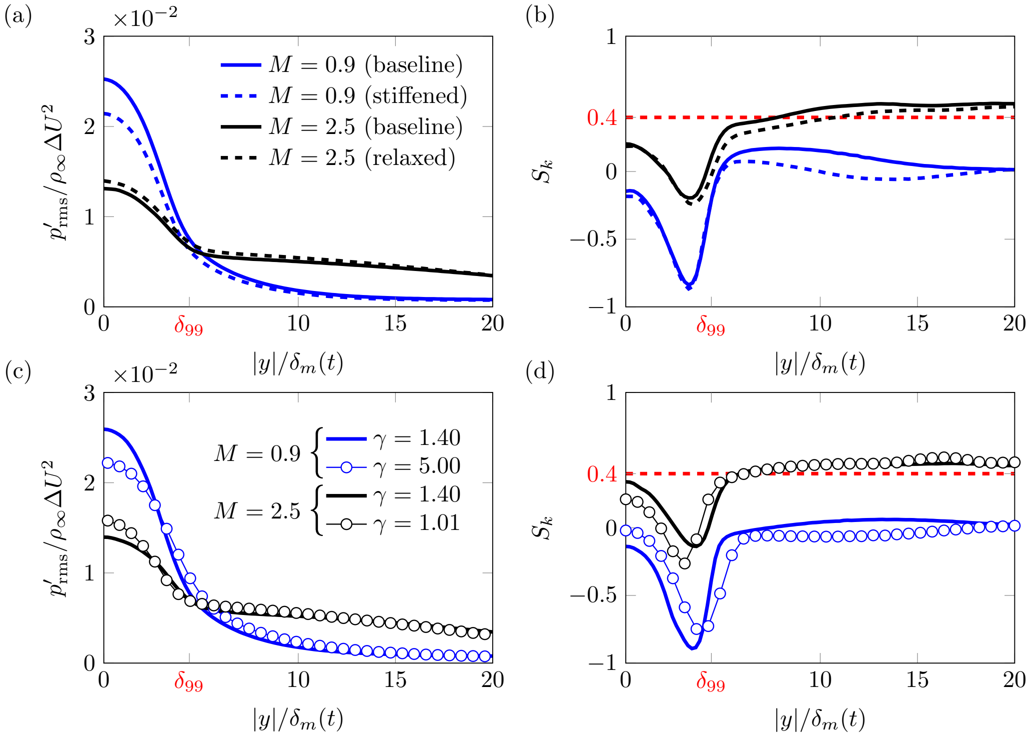

FIG. 13. Effect of gas stiffness on pressure (a) intensity and (b) skewness and the effect of γ on the pressure (c) intensity and (d) skewness.

that the turbulence intensity is insensitive to compressibility *per se*; instead, it depends mostly on finite speed of sound effects, which in turn depend on the Mach number M [48,52]. The radiated waves remain directional, though they are obviously thicker and weaker, especially for $\mu_b = 100\mu$. For $|y| \gtrsim 5\,\delta_m$ in Fig. 15, the bulk viscosity decreases the sound intensity and also its S_k, though S_k remains constant over the propagation range. For the same M and $M_t(y = 0)$, S_k is reduced for $\mu_b \gtrsim 10\mu$, supporting a link between the S_k and sound intensity via gas-dynamic compressibility.

V. GAS-DYNAMIC MECHANISMS

Sections III and IV showed that the signatures of nonlinear wave dynamics in the radiated pressure are insensitive to the turbulence structure and gas thermodynamic properties. Suppressing fluid dilatation significantly suppressed the radiation and near-field velocity divergence, but it did not alter the turbulence intensities. Together, these observations suggest that the wave features, including S_k, originate from nonlinear mechanisms distinct from turbulence hydrodynamics.

To isolate the underlying mechanisms, we appeal to the established simple case of steady supersonic flow adjacent to a wavy wall [36], which has been previously used in regard to sound generation by turbulence [15], and now includes quadratic nonlinearities. Figure 16 shows the basic configuration. The irrotational steady supersonic flow over a wavy wall at $y = \varepsilon g(x, z)$ in Fig. 16(a) has the boundary condition

$$\mathbf{u} \cdot \nabla S = 0, \tag{16}$$

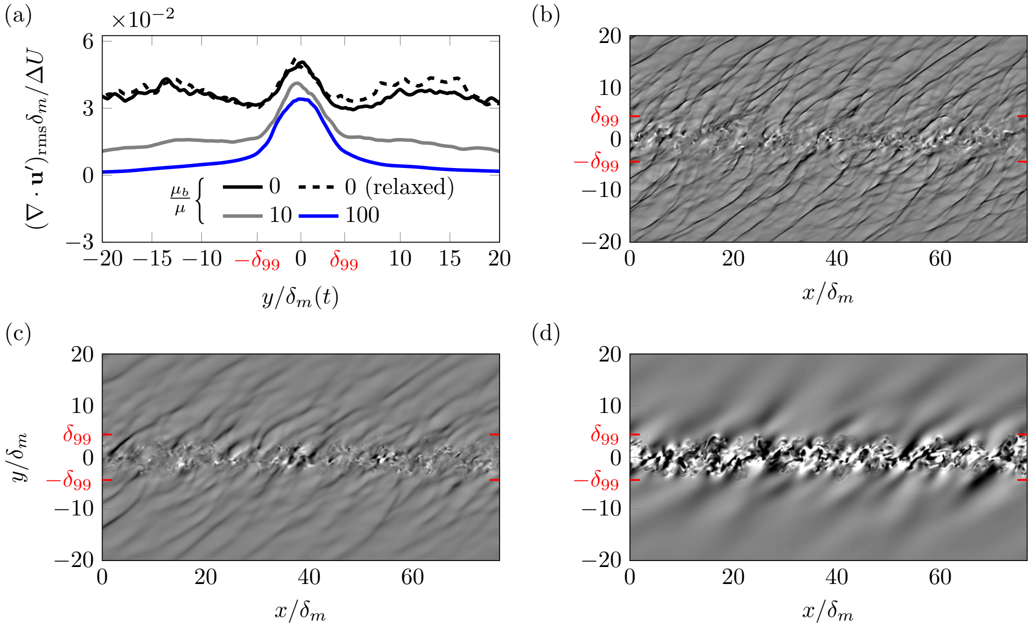

FIG. 14. (a) The effect of μ_b on the average dilatation intensity across the mixing layers. [(b)–(d)] Dilatation visualization at $z = L_z/2$ when $\delta_m/\delta_m^o = 10$: (b) $\mu_b/\mu = 0$, (c) 10, and (d) 100. The gray scale for panels (b) and (c) is $|\nabla \cdot \mathbf{u}| < 0.15\,\Delta U/\delta_m$ and (d) is $|\nabla \cdot \mathbf{u}| < 0.03\,\Delta U/\delta_m$, with black indicating compression.

where $S(\mathbf{x}) = y - \varepsilon g(x, z) = 0$. To order ε at $y = 0$, this boundary condition is [36,37]

$$\varphi_y = (1 + \varphi_x)\varepsilon g_x + \varphi_z \varepsilon g_z - \varphi_{yy}\varepsilon g, \tag{17}$$

where φ is a velocity potential such that $\mathbf{u} = U_\infty \nabla(x + \varphi)$. The corresponding first-order potential solution of the isentropic two-dimensional Euler equations is [18,36,53]

$$\varphi = -\frac{\varepsilon}{\sqrt{(M_\infty^2 - 1)}}\, g\big(x - y\sqrt{(M_\infty^2 - 1)}\big), \tag{18}$$

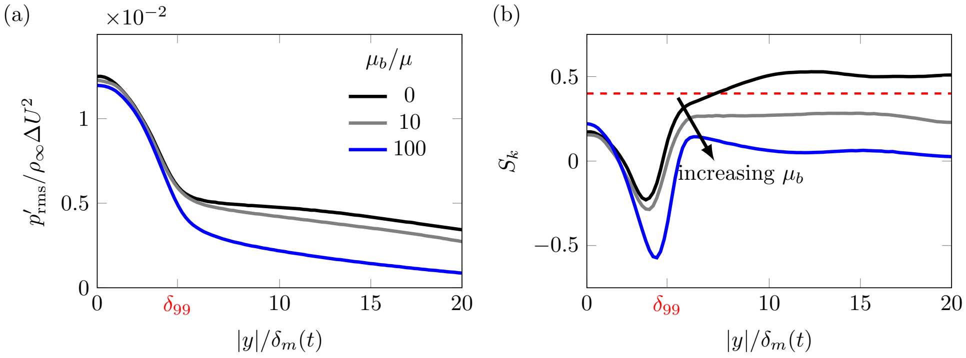

FIG. 15. Effect of bulk viscosity on the pressure (a) intensity and (b) skewness.

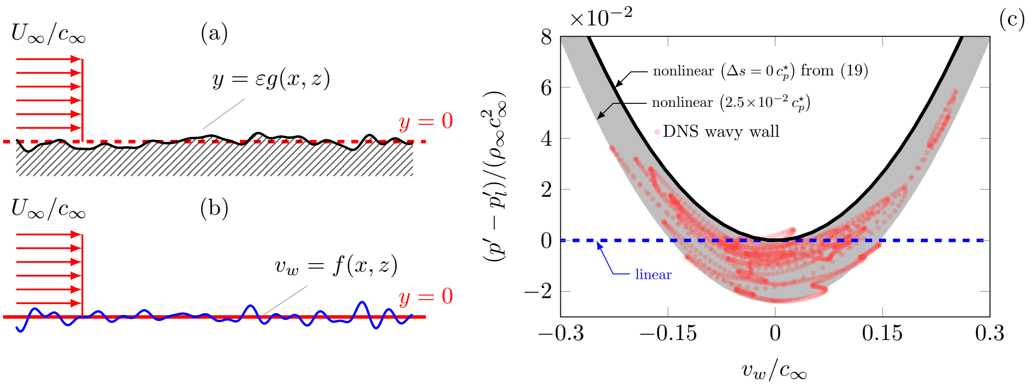

FIG. 16. Uniform flow adjacent to (a) a wavy wall and (b) a corresponding v-velocity distribution along $y = 0$. (c) The deviation of the boundary pressure distribution from the linear theory (p_l') for the two-dimensional wavy wall $M = 1.75$ shown in panels (a) and (b). Modifications to the model formulation for entropy change, $\Delta s = 2.5 \times 10^{-2}\, c_p^\star$, is shown for reference ($c_p^\star$ is the constant-pressure heat capacity).

and its normal velocity perturbations φ_y at the wall are proportional to the local slope of the wall εg_x. The bumps and depressions in the wall streamline generate disturbances that radiate along their characteristics with constant strength at the Mach angle $\theta = \sin^{-1}(1/M_\infty)$. Van Dyke [36] carried this analysis to order ε^2 using (17), which yields

$$\frac{p'}{\rho_\infty U_\infty^2} = \frac{\varepsilon g_x}{\sqrt{\left(M_\infty^2 - 1\right)}} + \frac{(\gamma+1)M_\infty^4 - 4\left(M_\infty^2 - 1\right)}{4\left(M_\infty^2 - 1\right)^2}(\varepsilon g_x)^2. \tag{19}$$

The solution, interpreted as a $y = 0$ boundary condition on v per (17), is visualized in Fig. 16(b) and provides the analogy we analyze. In particular, we recognize in (19) that the pressure has stronger $p' > 0$ peaks for $g_x > 0$ than corresponding $p' < 0$ for $g_x < 0$ and thus $S_k > 0$. This is quantified (relative to the linear solution) in Fig. 16(c) for $M_\infty = 1.75$ free-stream velocity. The DNS data, also shown in Fig. 16(c), tracks this behavior closely. Of course, the DNS is not exactly isentropic as is the model. Still, it all falls within a band, tracking the wavy-wall model. This band thickness matches the observed entropy extrema in the data ($\Delta s = 2.5 \times 10^{-2}\, c_p^\star$). This value from the DNS is used to anticipate the bounds displayed for the corresponding linear and order-ε^2 wavy-wall results.

An extension of the weakly nonlinear solution to three dimensions has not been found, so direct simulations are used, with turbulence-based velocities providing boundary data. The specific configuration is shown in Fig. 17 and solved using the same high-order finite-difference methods as for the corresponding turbulence DNS [12]. The computational domain is periodic in x and z with $L_x \times L_y \times L_z = (34.8 \times 20 \times 12.8)\,\delta_m$ and discretized with $N_x \times N_y \times N_z = 1536 \times 801 \times 512$ uniformly spaced mesh points. For $v_w = \varphi_y$ in (17), we use the $y = 0$ velocity from the turbulence DNS shown in Figs. 17(b)–17(d). The v' component defines the effective shape of the wall g to order ε, then with g, the $y = 0$ values for u' and w' and the normal derivative of v' form the remaining terms of the right side of (17). Though not shown here, the sound is insensitive to spatial structure of the wall, consistent with Sec. III and shown in more detail elsewhere [13]. Within this model, we can independently adjust both v_w perturbations and the free-stream momentum flux $\propto U_\infty$ to examine their respective roles in the near-field sound radiation.

For the free stream, the most obvious choice is $U_\infty = \Delta U/2$. However, this implies that the Mach waves are generated just at $y = 0$, although the advection of the average velocity perturbations follow closely to the local mean flow (with appropriate y dependence) [54], which is also shown in Appendix C for the current shear-layer configuration. Based on observed wave angle and the

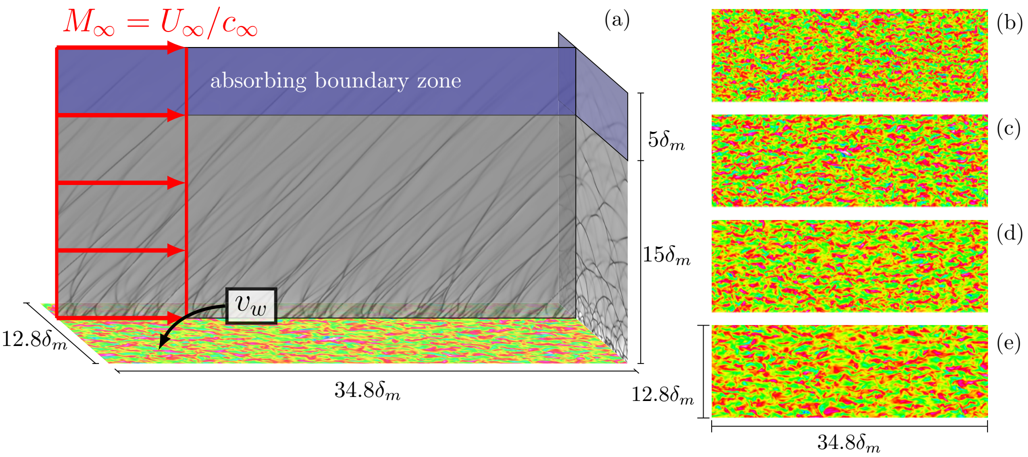

FIG. 17. (a) Computational domain of supersonic flow adjacent to a plane of cross-stream velocity fluctuations. Spatial distributions of v_w from (b) $M = 1.5$, (c) $M = 2.5$, (d) $M = 3.0$, and (e) $M = 3.5$ DNS of mixing layers colored from $-0.3 < v_w/\Delta U < 0.3$ velocities.

Mach-angle formula (1), we deduce an advection speed that is faster than would be anticipated for $M/2$ (or $\Delta U/2$) [12], similar to the observations of Oertel [14] in shear-layer turbulence. In those experiments, the speed of the structures correlated with

$$M_c = \frac{1}{2}\frac{(\Delta U + c_\infty)}{c_\infty}, \tag{20}$$

which also agrees with average wave angles near turbulence [12]. Thus, the free-stream Mach M_∞ is set using (20) for each mixing layer M as listed in Table II. Additional simulations are designed to assess sensitivity to this choice of M_∞ and implications for how this might influence the intensity and S_k. The v_w boundary condition at $y = 0$ is implemented using a standard simultaneous-approximation-term (SAT) approach designed for (17) [55]. The boundary at $y = L_y$ has a typical damping region that suppresses reflections into the domain [13]. The initial transient solution is integrated to steady state with a standard fourth-order Runge-Kutta scheme.

Figures 18(a) and 18(b) show that this kind of boundary condition and uniform advection produces an array of waves at Mach angle ($\theta \approx 35^\circ$) associated with the $M_\infty = 1.75$ used for this flow. The nominally linear field, shown in Fig. 18(a), computed by the same methods but with a factor of 10^{-4} reduced amplitude at $y = 0$, shows similar directional waves though these lack the shocklike structure of their nonlinear counterpart [Fig. 18(b)]. The compressions and expansions in this linear case also have approximately the same amplitude so $S_k \approx 0$. The waves in the DNS [Fig. 18(c)] are similarly directional, but as expected, due to the finite-time correlation of the turbulence, are finite along the wavefront. There are also additional perturbations between the obvious compressions due to the turbulence character of the source. Normal to the streamwise

TABLE II. Simulations of supersonic flow adjacent to wall-like disturbances.

M_∞	Figure 17 frame	$v_{\mathrm{rms}}/c_\infty$ of v_w
1.25	(b)	0.150
1.75	(c)	0.255
2.00	(d)	0.296
2.25	(e)	0.343

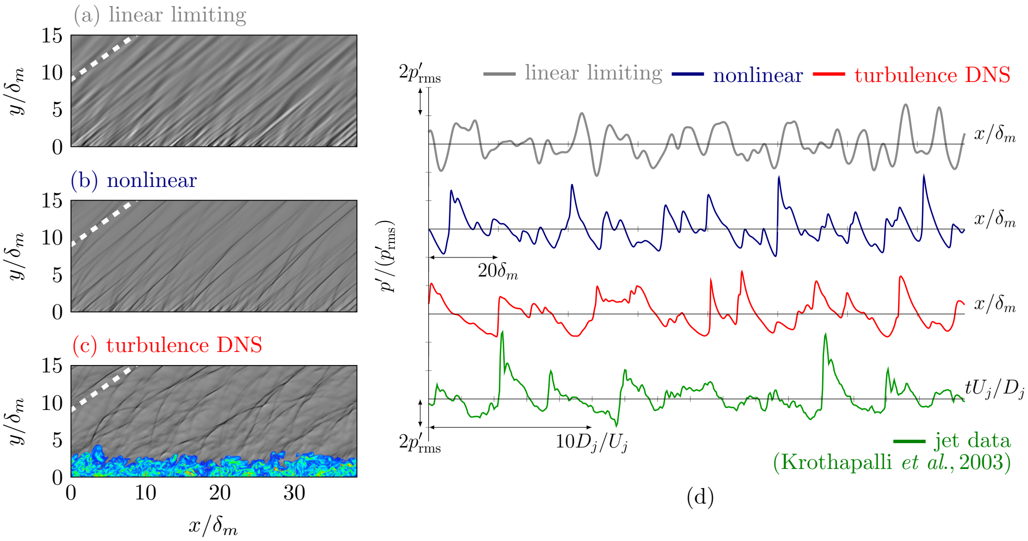

FIG. 18. Dilatation $|\nabla \cdot \mathbf{u}| < 0.1\,U_\infty/\delta_m$ at $z = L_z/2$ for the $M_\infty = 1.75/M = 2.5$ case: (a) linear, (b) nonlinear, and (c) turbulence DNS. The dashed line at 35° from the x axis indicates the nominal Mach angle. The color map in panel (c) correspond to $|\nabla \cdot\ \mathbf{u}| < 0.5\,\Delta U/\delta_m$. The dilatation in panel (a) has been scaled by 10^4. (d) Pressure traces for panels (a)–(c) at $y = 10\delta_m$ and data from a Mach 2 jet [57] at $r/D_j \approx 61$ (based on the jet diameter D_j and jet velocity U_j).

flow, Fig. 19 shows that the model also reproduces the three-dimensional Mach-wave structure from turbulence, with arched waves that cross one another. From this view, the limiting linear field [Fig. 19(a)] little resembles the turbulence DNS [Fig. 19(c)]. The qualitative similarities between the nonlinear model and the turbulence DNS is partly due to large-scale eddies being long lived compared to the acoustic timescales, which makes them more like stationary bumps. Turbulence integral timescales (Appendix C) relative to the acoustics confirms its slow evolution. Furthermore, perturbations in high-Mach-number flow are more acoustically efficient than in subsonic flow,

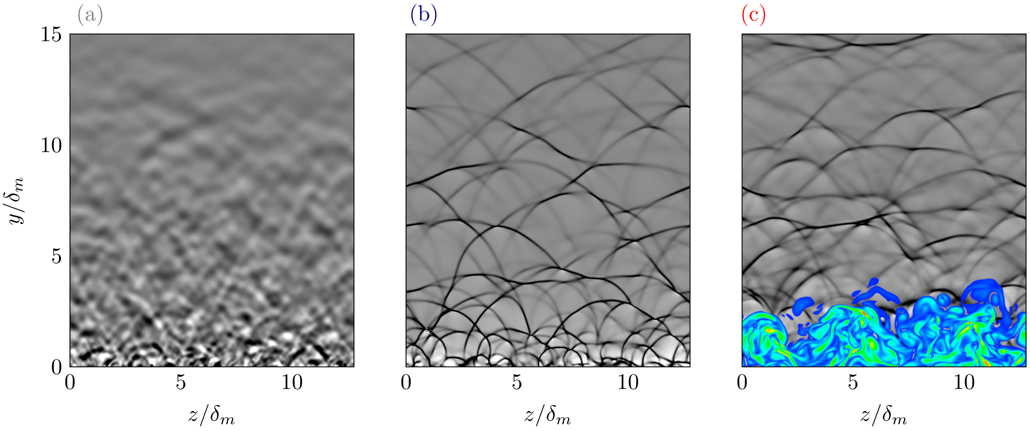

FIG. 19. Streamwise view of dilatation $|\nabla \cdot \mathbf{u}| < 0.1\Delta U/\delta_m$ at $z = L_z/2$ for the steady $M = 1.75$ (a) linear and (b) nonlinear model and (c) $y > 0$ from the DNS $M = 2.5$. The color map in panel (c) corresponds to $|\nabla \cdot \mathbf{u}| < 0.5\Delta U/\delta_m$. The dilatation in panel (a) has been scaled by 10^4.

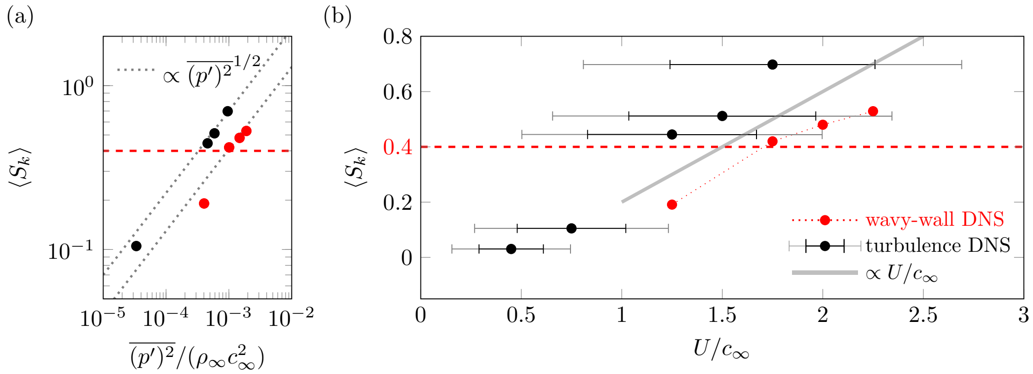

FIG. 20. Domain average skewness dependence on the (a) acoustic intensity at $|y| = 20\delta_m$ and (b) the flow velocity U. The dotted lines in panel (a), $\propto \overline{(p')^2}^{1/2}$, are separated by a factor of two in the pressure intensity. In panel (b), for the wavy-wall model, the $U/c_\infty = M_\infty$ are listed in Table II. For turbulence, an anticipated range of advection velocities are based on y-location mean speed $\bar{u}(y)$ (see Sec. II). The results are shown for $U = \Delta U/2 - \bar{u}(y)$: $y = 0$ (symbol), $y = \pm 1\delta_m$ (inner bar), and $y = \pm 2\delta_m$ (outer bar).

and their radiation is relatively insensitive to the time dependence of their source [24,56], which facilitates further comparison between the turbulence and the steady-flow model to examine its mechanisms.

In Fig. 18(d), the p' peaks of the linear-limiting case have similar magnitude and rounded shape as the troughs; however, the nonlinear model flow reproduces the steep compressions followed by shallower, rounded expansions seen in the DNS. This figure also includes data from a Mach 2 jet [57], showing the similarity with the computed pressure traces. The sharp compressions reach $\approx 4\, p'_{\text{rms}}$, consistent with measurements [4,58,59] and simulations [60] of jets. The domain average S_k,

$$\langle S_k \rangle = \frac{1}{L_y - w} \int_{y=0}^{L_y - w} S_k(y)\, dy, \tag{21}$$

neglecting the absorbing-sponge region ($w = 5\,\delta_m$), is shown in Fig. 20. Like the turbulence DNS, it increases approximately linearly with p'_{rms} and also with M_∞. The trend and magnitude of S_k for $1.25 \lesssim M_\infty \lesssim 2$ also agrees with those observed in the turbulent mixing layers. On the other hand, for the $M = 3.5$ turbulence, the model underpredicts S_k using advection speed (20). This might suggest that larger advection speeds in the $M = 3.5$ turbulence are causing larger S_k, which is possible since Machlike waves were observed at even shallower angles than those corresponding to speeds in (20) [12].

Both the two-dimensional (19) and the three-dimensional model flows show that S_k can arise from both finite-fluctuation amplitudes $\sim(\varepsilon g_x)^2$ and the free-stream momentum flux $\sim M_\infty$. These are shown separately in Fig. 21. The S_k increases with M_∞, up to $S_k \approx 0.4$ for $M_\infty \gtrsim 1.5$ in Fig. 21(a). Rescaling v_w at fixed M_∞ shows the $\langle S_k \rangle < 0.4$ for $v_{\text{rms}}/c_\infty < 0.2$ so turbulence-like fluctuation levels are necessary to support the nonlinearity producing the observed S_k. The approximate linear growth of S_k in Fig. 21(b) with v_{rms} for $0 < v_{\text{rms}}/c_\infty < 0.2$ is also consistent with instability amplitude dependence in Figs. 3(c) and 3(d). Dissipation mechanisms suppress S_k in the sound field [12], which likely contributes to the leveling off of S_k for the more intense waves, while for the inviscid model (19), S_k would increase with M_∞.

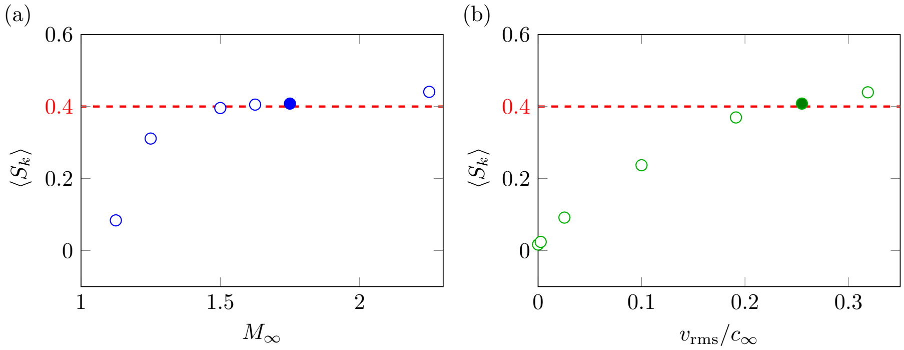

FIG. 21. Two routes to increasing S_k in the model flow: (a) due to mean flow M_∞ and (b) due to fluctuation intensity $v_{\rm rms}/c_\infty$. Filled symbols indicate the reference case in Table II, $M_\infty = 1.75$ and $v_{\rm rms}/c_\infty = 0.255$, based on a corresponding $M = 2.5$ turbulence case.

VI. CONCLUSIONS

The main conclusion of this paper is that the peculiarly asymmetric pressure amplitudes with $S_k \gtrsim 0.4$ arise from a nonlinear gas-dynamic effect near, yet only one-way coupled, to the turbulence source. A second-order extension of a wavy-wall model shows this in two dimensions; a three-dimensional direct numerical simulation with a boundary condition in the same asymptotic limit and based on a frozen turbulence field reproduces all the key features: S_k values, Mach waves in x-y planes, curved and intersected shocklike waves in z-y planes, and intensity to within a factor of 2. The root of the S_k behavior is the nonlinearity intrinsic in gas dynamics. The usual assumption that sound does not significantly affect the turbulence, which is a lynchpin of analysis of aerodynamic sound at lower speeds [6,7], is needed to make this statement, and this was confirmed by strongly suppressing the amplitude and shocklike character of the radiation with elevated bulk viscosity. Similarly, the turbulence was insensitive to the gas stiffness, so long as the momentum fluxes were set to match the baseline flows. We similarly confirm that the key observations coincide with the nonlinear saturation of linear instabilities, and simulations with source terms designed to alter the turbulence structure show that it is not of primary importance for the observations. It is instead a consequence of finite-amplitude disturbances with relative supersonic advection speed.

ACKNOWLEDGMENT

Support by AFOSR (No. FA9550-10-1-0432) is gratefully acknowledged.

APPENDIX A: SUMMARY OF INSTABILITY-SATURATION SIMULATIONS

The results presented in Sec. II summarized the main results from many simulations. The parameters of these simulations are shown in Table III for reference and completeness.

APPENDIX B: SOUND SOURCES FROM ARTIFICAL SOURCE TERMS

For the simulations of Sec. III, to which sources are added to alter the turbulence structure, it is important to assess the direct consequences of these artificial additions as direct acoustic sources. To do this, we rearrange the governing equations, following the usual approach of formulating an acoustic analogy [6], to form

$$\frac{\partial^2 \rho}{\partial t^2} - a_o^2 \frac{\partial^2 \rho}{\partial x_i \partial x_i} = \frac{\partial^2 T_{ij}}{\partial x_i \partial x_j} + \frac{\partial \mathcal{M}}{\partial t} - \frac{\partial F_i}{\partial x_i}, \tag{B1}$$

TABLE III. Simulation parameters of unstable modes.

M	α	β	θ	ω_i	ω_r/α	U_c/c_∞
0.9	0.78	0.00	0	0.28	0.00	0.45
0.9	0.78	0.26	18	0.27	0.00	0.43
0.9	0.78	0.49	32	0.25	0.00	0.38
0.9	0.78	0.62	38	0.23	0.00	0.35
0.9	0.78	0.69	41	0.22	0.00	0.34
0.9	0.78	0.90	49	0.18	0.00	0.30
1.5	0.55	0.01	2	0.16	0.00	0.75
1.5	0.55	0.04	5	0.16	0.00	0.75
1.5	0.55	0.10	11	0.16	0.00	0.74
1.5	0.55	0.15	15	0.17	0.00	0.72
1.5	0.55	0.20	20	0.17	0.00	0.71
1.5	0.55	0.25	24	0.17	0.00	0.68
1.5	0.55	0.33	31	0.17	0.00	0.65
1.5	0.55	0.39	35	0.18	0.00	0.61
1.5	0.55	0.48	41	0.18	0.00	0.56
1.5	0.55	0.57	46	0.17	0.00	0.52
1.5	0.55	0.67	51	0.16	0.00	0.48
1.5	0.55	0.79	55	0.15	0.00	0.43
1.5	0.55	0.94	60	0.13	0.00	0.38
1.5	0.55	1.22	66	0.08	0.00	0.31
2.5	0.29	0.01	2	0.02	−0.27	1.51
2.5	0.29	0.11	21	0.02	−0.22	1.37
2.5	0.29	0.16	29	0.02	−0.18	1.25
2.5	0.29	0.19	34	0.02	−0.14	1.16
2.5	0.29	0.23	38	0.02	−0.07	1.04
2.5	0.29	0.24	40	0.03	0.00	0.96
2.5	0.29	0.28	44	0.06	0.00	0.90
2.5	0.29	0.31	47	0.07	0.00	0.86
2.5	0.29	0.33	49	0.08	0.00	0.82
2.5	0.29	0.37	52	0.08	0.00	0.78
2.5	0.29	0.40	54	0.09	0.00	0.73
2.5	0.29	0.43	56	0.09	0.00	0.70
2.5	0.29	0.46	58	0.09	0.00	0.67
2.5	0.29	0.48	59	0.10	0.00	0.64
2.5	0.29	0.52	61	0.10	0.00	0.61
2.5	0.29	0.56	63	0.10	0.00	0.57
2.5	0.29	0.59	64	0.10	0.00	0.55
2.5	0.29	0.61	64	0.09	0.00	0.54
2.5	0.29	0.64	66	0.09	0.00	0.51
2.5	0.29	0.68	67	0.09	0.00	0.49
2.5	0.29	0.72	68	0.09	0.00	0.46
2.5	0.29	0.74	69	0.09	0.00	0.45
3.5	0.23	0.04	9	0.01	−0.45	2.17
3.5	0.23	0.13	31	0.01	−0.38	1.84
3.5	0.23	0.22	44	0.01	−0.30	1.48
3.5	0.23	0.25	48	0.01	−0.26	1.35
3.5	0.23	0.29	52	0.01	−0.21	1.22
3.5	0.23	0.33	56	0.01	−0.15	1.07
3.5	0.23	0.31	54	0.01	−0.18	1.14
3.5	0.23	0.32	54	0.01	−0.17	1.12

TABLE III. (*Continued.*)

M	α	β	θ	ω_i	ω_r/α	U_c/c_∞
3.5	0.23	0.36	58	0.01	0.00	0.93
3.5	0.23	0.37	59	0.03	0.00	0.90
3.5	0.23	0.39	60	0.03	0.00	0.88
3.5	0.23	0.41	61	0.04	0.00	0.85
3.5	0.23	0.42	62	0.04	0.00	0.82
3.5	0.23	0.44	63	0.05	0.00	0.79
3.5	0.23	0.46	64	0.05	0.00	0.77
3.5	0.23	0.48	65	0.05	0.00	0.74

where $\mathcal{M}$ and $\mathcal{F}$ are the effective mass and momentum sources due to the additional term, and $T_{ij} = \rho u_i u_j - \sigma_{ij} + (p - a_o^2\rho)\delta_{ij}$ is the usual Lighthill stress. Of course, the added sources also alter T_{ij}, so T_{ij}^o designates the corresponding Lighthill stress for unforced turbulence, with $\mathcal{M} = 0$ and $\mathcal{F}_i = 0$. The space-time average of the sources in (B1) are shown in Fig. 22. Unlike low-Mach-number flow, we are not in a compact-source regime, and there is no expectation of a quadrupolar (or similar canceling polar character), which would significantly suppress the efficiency of T_{ij} as a sound source, so we simply make a direct comparison. The acoustic sources due to the added mass and momentum sources are small compared to the Reynolds stresses in T_{ij}. For $y \lesssim 5\delta_m$, the $|(T_{ij})_{ij} - (T_{ij}^o)_{ij}| > |(\mathcal{M})_t| + |(\mathcal{F}_i)_i|$ result suggests that any change in the sound arises from turbulence T_{ij} modifications, which results in Sec. III confirm do not change significantly.

APPENDIX C: TURBULENCE ADVECTION SPEED

To examine advection velocities in high-speed free-shear turbulence, we use the space-time correlation of streamwise velocity perturbations

$$C_{xt}(\Delta_x, \Delta_t, y) = \frac{\overline{u'(x, y, z, t)u'(x + \Delta_x, y, z, t + \Delta_t)}}{\overline{u'(x, y, z, t)u'(x, y, z, t)}}, \tag{C1}$$

some of which are shown in Fig. 23(a) for $M = 2.5$. Figure 23(b) shows an integral space-time scale defined by

$$\mathcal{L}(\mathcal{U}, y) = \int C_{xt}(\mathcal{U}\Delta_t, \Delta_t, y)\, d\Delta_t, \tag{C2}$$

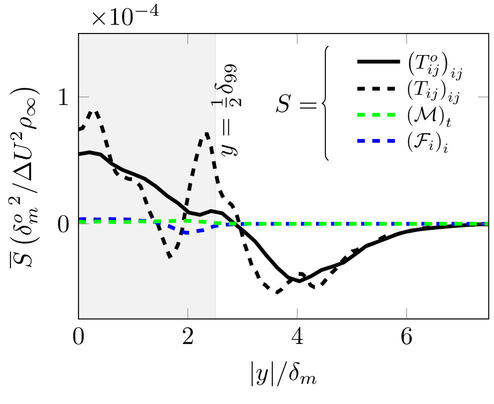

FIG. 22. The effect of turbulence modification for $A = 2$ on acoustic sources.

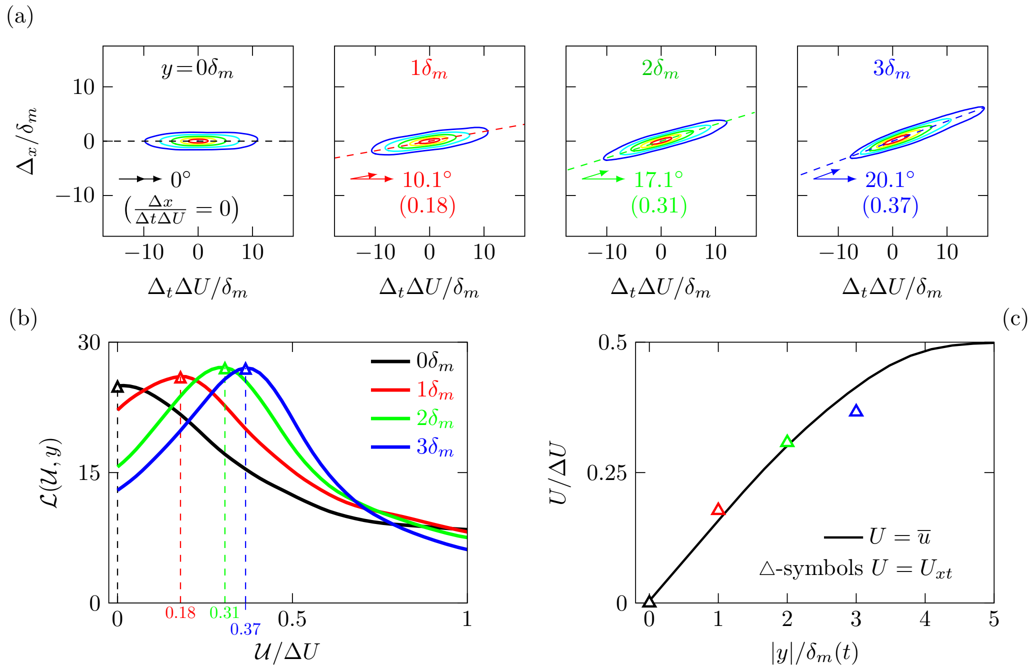

FIG. 23. (a) Space-time correlations of streamwise velocity perturbations for $M = 2.5$ between $0 \leqslant y/\delta_m \leqslant 3$. Five levels indicate normalized correlations from $0.5 \leqslant C_{xt} \leqslant 0.9$ and dashed lines indicate the direction along the maximum integral space-time scale shown in panel (b) with the maximum indicated by triangles. (c) The advection velocity based on the direction of maximum integral space-time correlation compared to the mean streamwise velocity.

which is parameterized by velocity $\mathcal{U} = \Delta x/\Delta t$. The $\mathcal{U}$ that maximizes (C2), U_{xt}, is confirmed to agree with the orientation of correlation contours in Fig. 23(a). Because of the symmetry of the flow, the same space-time advection velocities, with opposite sign, are found for $y < 0$. Shown in Fig. 23(c), this deduced turbulence speed at discrete y is close to the local mean streamwise velocity profile, $U_{xt} \approx \overline{u}$, which is similar to behavior observed in simulated boundary layer turbulence [61]. Similar results confirm that this behavior holds for the range of $0.9 \lesssim M \lesssim 3.5$ of interest here.

[1] S. R. Pate and C. J. Schueler, Radiated aerodynamic noise effects on boundary-layer transition in supersonic and hypersonic wind tunnels, AIAA J. **7**, 450 (1969).

[2] J. Laufer, Aerodynamic noise in supersonic wind tunnels, J. Aerosp. Sci. **28**, 685 (1961).

[3] M. V. Lowson and J. B. Ollerhead, Visualization of noise from cold supersonic jets, J. Acoust. Soc. Am. **44**, 624 (1968).

[4] A. Krothapalli, L. Venkatakrishnan, and L. Lourenco, Crackle: A dominant component of supersonic jet mixing noise, in *Sixth AIAA/CEAS Aeroacoustics Conference* (2000), pp. 2000–2024.

[5] J. E. Ffowcs Williams, The noise from turbulence convected at high speed, Philos. Trans. R. Soc. London, Ser. A **255**, 469 (1963).

[6] D. G. Crighton, Basic principles of aerodynamic noise generation, Progr. Aerospace Sci. **16**, 31 (1975).

[7] M. J. Lighthill, On sound generated aerodynamically. I: General theory, Proc. R. Soc. London, Ser. A **211**, 564 (1952).

[8] O. M. Phillips, On the generation of sound by supersonic turbulent shear layers, J. Fluid Mech. **9**, 1 (1960).

[9] N. E. Murray and G. W. Lyons, On the convection velocity of source events related to supersonic jet crackle, J. Fluid Mech. **793**, 477 (2016).

[10] D. K. Mclaughlin, G. L. Morrison, and T. R. Troutt, Experiments on the instability waves in a supersonic jet and their acoustic radiation, J. Fluid Mech. **69**, 73 (1975).

[11] J. M. Seiner, M. K. Ponton, B. J. Jansen, and N. T. Lagen, The effects of temperature on supersonic jet noise emission, DGLR/AIAA 14th Aeroacoustics Conference: May 11-14, 1992, Eurogress Center Aachen, Federal Republic of Germany, DGLR/AIAA Paper 92-02-046, 1992.

[12] D. A. Buchta and J. B. Freund, The near-field pressure radiated by planar high-speed free-shear-flow turbulence, J. Fluid Mech. **832**, 383 (2017).

[13] D. A. Buchta, Crackle noise from high-speed free-shear-flow turbulence, Ph.D. thesis, University of Illinois at Urbana-Champaign, Urbana, IL, 2016.

[14] H. Oertel, Kinematics of Mach waves inside and outside supersonic jets, in *Recent Developments in Theoretical and Experimental Fluid Mechanics*, edited by U. Müller, K. G. Roesner, and B. Schmidt (Springer, Berlin, 1979), pp. 121–136.

[15] C. K. W. Tam, Directional acoustic radiation from a supersonic jet generated by shear layer instability, J. Fluid Mech. **46**, 757 (1971).

[16] J. E. Ffowcs Williams, J. Simson, and V. J. Virchis, “Crackle”: An annoying component of jet noise, J. Fluid Mech. **71**, 251 (1975).

[17] K. L. Gee, V. W. Sparrow, A. Atchley, and T. B. Gabrielson, On the perception of crackle in high-amplitude jet noise, AIAA J. **45**, 593 (2007).

[18] G. B. Whitham, *Linear and Nonlinear Waves* (John Wiley & Sons, New York, 1974).

[19] E. Mollo–Christensen, Jet noise and shear flow instability seen from an experimenter’s viewpoint, J. Appl. Mech. **34**, 1 (1967).

[20] D. G. Crighton and P. Huerre, Shear-layer pressure fluctuations and superdirective acoustic sources, J. Fluid Mech. **220**, 355 (1990).

[21] P. Jordan and T. Colonius, Wave packets and turbulent jet noise, Annu. Rev. Fluid Mech. **45**, 173 (2013).

[22] V. Chobotov and A. Powell, On the prediction of acoustic environments from rockets, Tech. Rep. E.M.-7-7, Ramo-Wooldridge Corporation, 1957 (unpublished).

[23] H. K. Tanna, P. D. Dean, and R. H. Burrin, The Generation and Radiation of Supersonic Jet Noise, Volume 3, Turbulent Mixing Noise Data, Lockheed-Georgia Co Marietta (1976).

[24] A. V. G. Cavalieri, P. Jordan, A. Agarwal, and Y. Gervais, Jittering wave-packet models for subsonic jet noise, J. Sound Vib. **330**, 4474 (2011).

[25] D. Obrist, Directivity of acoustic emissions from wave packets to the far field, J. Fluid Mech. **640**, 165 (2009).

[26] C. K. W. Tam and D. E. Burton, Sound generated by instability waves of supersonic flows. Part I. Two-dimensional mixing layers, J. Fluid Mech. **138**, 249 (1984).

[27] C. K. W. Tam and D. E. Burton, Sound generated by instability waves of supersonic flows. Part II. Axisymmetric jets, J. Fluid Mech. **138**, 273 (1984).

[28] L. C. Cheung and S. K. Lele, Linear and nonlinear processes in two-dimensional mixing layer dynamics and sound radiation, J. Fluid Mech. **625**, 321 (2009).

[29] A. Sinha, D. Rodriguez, G. A. Brés, and T. Colonius, Wavepacket models for supersonic jet noise, J. Fluid Mech. **742**, 71 (2014).

[30] K. Mohseni, T. Colonius, and J. B. Freund, An evaluation of linear instability waves as sources of sound in a supersonic turbulent jet, Phys. Fluids **14**, 3593 (2002).

[31] M. J. Lighthill, Viscosity effects in sound waves of finite amplitude, in *Surveys in Mechanics*, edited by G. K. Batchelor and R. M. Davies (Cambridge University Press, Cambridge, UK, 1956), pp. 250–351.

[32] D. G. Crighton, Model equations of nonlinear acoustics, Annu. Rev. Fluid Mech. **11**, 11 (1979).

[33] J. B. Freund, S. K. Lele, and P. Moin, Numerical simulation of a Mach 1.92 turbulent jet and its sound field, AIAA J. **38**, 2023 (2000).

[34] N. de Cacqueray and C. Bogey, Noise of an overexpanded Mach 3.3 jet: Non-linear propagation effects and correlations with flow, Int. J. Aeroacoustics **13**, 607 (2014).

[35] C. K. W. Tam, Supersonic jet noise, Annu. Rev. Fluid Mech. **27**, 17 (1995).

[36] M. D. Van Dyke, Study of second-order supersonic-flow theory, Technical Report 1081, National Advisory Committee for Aeronautics (1951), pp. 489–511.

[37] M. J. Lighthill, Higher approximations, in *General Theory of High Speed Aerodynamics*, edited by W. R. Sears (Princeton University Press, Princeton, NJ, 1954), Sec. E.

[38] O. Rudenko, S. Gurbatov, and C. Hedberg, *Nonlinear Acoustics through Problems and Examples* (Trafford, Victoria, BC, 2010).

[39] E. J. Avital, R. E. Musafir, and T. Korakianitis, Nonlinear propagation of sound emitted by high speed wave packets, J. Comput. Acoustics **21**, 1250027-1 (2013).

[40] M. Lessen, J. A. Fox, and H. M. Zien, On the inviscid stability of the laminar mixing of two parallel streams of a compressible fluid, J. Fluid Mech. **23**, 355 (1965).

[41] T. L. Jackson and C. E. Grosch, Inviscid spatial stability of a compressible mixing layer, J. Fluid Mech. **208**, 609 (1989).

[42] N. D. Sandham and W. C. Reynolds, Compressible mixing layer: Linear theory and direct simulation, AIAA J. **28**, 618 (1990).

[43] E. J. Avital, N. D. Sandham, and K. H. Lou, Mach wave radiation by mixing layers. Part I: Analysis of the sound field, Theor. Comput. Fluid Dyn. **12**, 73 (1998).

[44] J. Jimenez and A. Pinelli, The autonomous cycle of near-wall turbulence, J. Fluid Mech. **389**, 335 (1999).

[45] T. R. Troutt and D. K. Mclaughlin, Experiments on the flow and acoustic properties of a moderate-Reynolds-number supersonic jet, J. Fluid Mech. **116**, 123 (1982).

[46] M. Samimy, J. H. Kim, M. Kearney-Fischer, and A. Sinha, Acoustic and flow fields of an excited high Reynolds number axisymmetric supersonic jet, J. Fluid Mech. **656**, 507 (2010).

[47] R. Kleinman and J. B. Freund, The sound from mixing layers simulated with different ranges of turbulence scales, Phys. Fluids **20**, 101503 (2008).

[48] C. Pantano and S. Sarkar, A study of compressibility effects in the high-speed turbulent shear layer using direct simulation, J. Fluid Mech. **451**, 329 (2002).

[49] M. S. Cramer, Numerical estimates for the bulk viscosity of ideal gases, Phys. Fluids **24**, 066102 (2012).

[50] M. S. Cramer and F. Bahmani, Effect of large bulk viscosity on large-Reynolds-number flows, J. Fluid Mech. **751**, 142 (2014).

[51] S. Pan and E. Johnsen, The role of bulk viscosity on the decay of compressible, homogeneous, isotropic turbulence, J. Fluid Mech. **833**, 717 (2017).

[52] J. B. Freund, S. K. Lele, and P. Moin, Compressibility effects in a turbulent annular mixing layer. Part 1. Turbulence and growth rate, J. Fluid Mech. **421**, 229 (2000).

[53] H. W. Liepmann and A. Roshko, *Elements of Gas Dynamics*, Dover Books on Aeronautical Engineering Series (Dover, New York, 1957).

[54] G. S. Elliott, M. Samimy, and S. A. Arnette, The characteristics and evolution of large-scale structures in compressible mixing layers, Phys. Fluids **7**, 864 (1995).

[55] M. H. Carpenter, D. Gottlieb, and S. Abarbanel, Time-stable boundary conditions for finite-difference schemes solving hyperbolic systems: Methodology and application to high-order compact schemes, J. Comput. Phys. **111**, 220 (1994).

[56] N. D. Sandham, C. L. Morfey, and Z. W. Hu, Sound radiation from exponentially growing and decaying surface waves, J. Sound Vib. **294**, 355 (2006).

[57] A. Krothapalli, V. Arakeri, and B. Greska, Mach wave radiation: A review and an extension, In *41st Aerospace Sciences Meeting and Exhibit*, 2003.

[58] D. Papamoschou and M. Debiasi, Directional suppression of noise from a high-speed jet, AIAA J. **39**, 380 (2001).

[59] W. J. Baars and C. E. Tinney, Shock-structures in the acoustic field of a Mach 3 jet with crackle, J. Sound Vib. **333**, 2539 (2014).

[60] J. W. Nichols, S. K. Lele, F. E. Ham, S. Martens, and J. T. Spyropoulos, Crackle noise in heated supersonic jets, J. Eng. Gas Turbines Power **135**, 051202 (2013).

[61] J. Kim and F. Hussain, Propagation velocity of perturbations in turbulent channel flow, Phys. Fluids A **5**, 695 (1992).